Engineering Geology 314 (2023) 106970

Contents lists available at ScienceDirect

Engineering Geology

journal homepage: www.elsevier.com/locate/enggeo

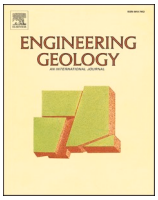

A site-specific earthquake ground response analysis using a fault-based approach and nonlinear modeling: The Case Pente site (Sulmona, Italy)

Paola Bordoni [a,*], Stefano Gori [a], Aybige Akinci [a], Francesco Visini [b], Sara Sgobba [c], Francesca Pacor [c], Fabrizio Cara [a], Stefano Pampanin [d], Giuliano Milana [a], Carlo Doglioni [a]

[a] Istituto Nazionale di Geofisica e Vulcanologia, Roma, Italy
[b] Istituto Nazionale di Geofisica e Vulcanologia, Pisa, Italy
[c] Istituto Nazionale di Geofisica e Vulcanologia, Milano, Italy
[d] Sapienza University of Rome, Department of Structural and Geotechnical Engineering, Italy

ARTICLE INFO

Keywords:
Seismogenic Structure
Near-fault Ground Motion
Seismic Hazard Analysis
Non-linear Dynamic Analysis
Seismic Amplification
Seismic Action

ABSTRACT

In this paper we present the ground response analyses (GRA) of a site where an industrial facility is planned. Due to its location on an active normal fault system known as a relevant seismic gap, the Mt. Morrone Fault system (MMF), and at the edge of a basin filled with slow velocity continental deposits, a inter-disciplinary and non-standard approach has been applied to assess the seismic input of the dynamic numerical analyses. It includes geological, seismological, geotechnical and engineering contributions. Two fault scenarios, MMF1 and MMF2, were considered and scenario-based (SSHA) and probabilistic (time-dependent, TD, and time-independent, TI) seismic hazard (PSHA) analyses were implemented. Comparison among the spectra corresponding to the 90th percentile of the SSHA statistical distribution and the PSHA average ones shows that the SSHA MMF2 has values similar to the PSHA TD model. The SSHA 90th percentile distribution was selected as target spectra to retrieve the seismic input for GRA. Nonlinear numerical simulations of seismic wave propagation were implemented to derive surface ground motion parameters. GRA acceleration response spectra and their PGA are notably higher, and thus on the side of safety, than those obtained following the Italian code approach for seismic resistant buildings. These results confirm that a scenario-based methodology can better capture the shaking effect in near-field conditions, avoiding possibly unconservative underestimations of the seismic actions and in view of a more robust performance-based approach used by engineers for either new design and/or assessment/retrofit purposes of the built environment.

1. Introduction

The site-specific analysis of the ground response to earthquakes (GRA) requires the evaluation of the amplification effect of local geology on the surface ground motion using numerical modeling of wave propagation. The output provides information on the ground surface seismic shaking in terms of time-histories and response spectra for seismic engineering design, in order to assess the performance of a structure and mitigate its seismic risk. The term local geology summarizes the contribution of several physical processes in action: from the effect of the impedance contrasts between superficial soft sediments and the underlying stiff deposits within a unidimensional horizontally layered scheme (lithostratigraphic effect), to the bidimensional and three-dimensional effects occurring in sediment-filled valley where body waves, entering the valley from the edges, are converted to locally generated surface waves by the sloping boundaries (e.g. Bard and Bouchon, 1980a, 1980b; Bard and Bouchon, 1985; Kawase and Aki, 1989; Olsen and Schuster, 1995; Komatitsch and Vilotte, 1998; Haines et al., 2004; Bordoni et al., 2010).

The Italian building code for seismic design and assessment of constructions (NTC2018, Norme Tecniche per le Costruzioni, 2018) requires, for the implementation of a GRA, the selection of the seismic motion for a set of performance limit states for the building/construction, based on the reference seismic hazard model on rock, the MPS04

* Corresponding author.
E-mail addresses: paola.bordoni@ingv.it (P. Bordoni), stefano.gori@ingv.it (S. Gori), aybige.akinci@ingv.it (A. Akinci), francesco.visini@ingv.it (F. Visini), sara.sgobba@ingv.it (S. Sgobba), francesca.pacor@ingv.it (F. Pacor), fabrizio.cara@ingv.it (F. Cara), stefano.pampanin@uniroma1.it (S. Pampanin), giuliano.milana@ingv.it (G. Milana), carlo.doglioni@ingv.it (C. Doglioni).

https://doi.org/10.1016/j.enggeo.2022.106970
Received 14 March 2022; Received in revised form 13 September 2022; Accepted 11 December 2022
Available online 14 December 2022

model (Modello di Pericolosità Sismica 2004, Montaldo et al., 2007, Stucchi et al., 2011) developed according to a probabilistic seismic hazard assessment (PSHA) approach (Cornell, 1971; McGuire, 1976; Bommer and Abrahamson, 2006).

The PSHA approach inherently does not represent the ground acceleration and related response spectra of an individual seismogenic source, but takes into account the contribution of all the sources with their magnitudes and distances, weighted according to the total probability theorem. In the case of PSHA based on seismic source zones, like the MPS04 model, it is expected that accelerations corresponding to common return periods for design can be exceeded.

This occurred particularly in the epicentral area of the 2016–2017 Central Italy, the 2012 Emilia-Northern Italy and the 2009 L'Aquila earthquakes (Stucchi et al., 2011; Luzi et al., 2017; Meletti et al., 2016; Panza and Bela, 2020) raising concerns. According to some authors (Cito and Iervolino, 2020 and references therein), this is a characteristic and not necessarily evidence of the failure of the PSHA. As the extension of the exceeding area in the epicentral area is between hundreds of

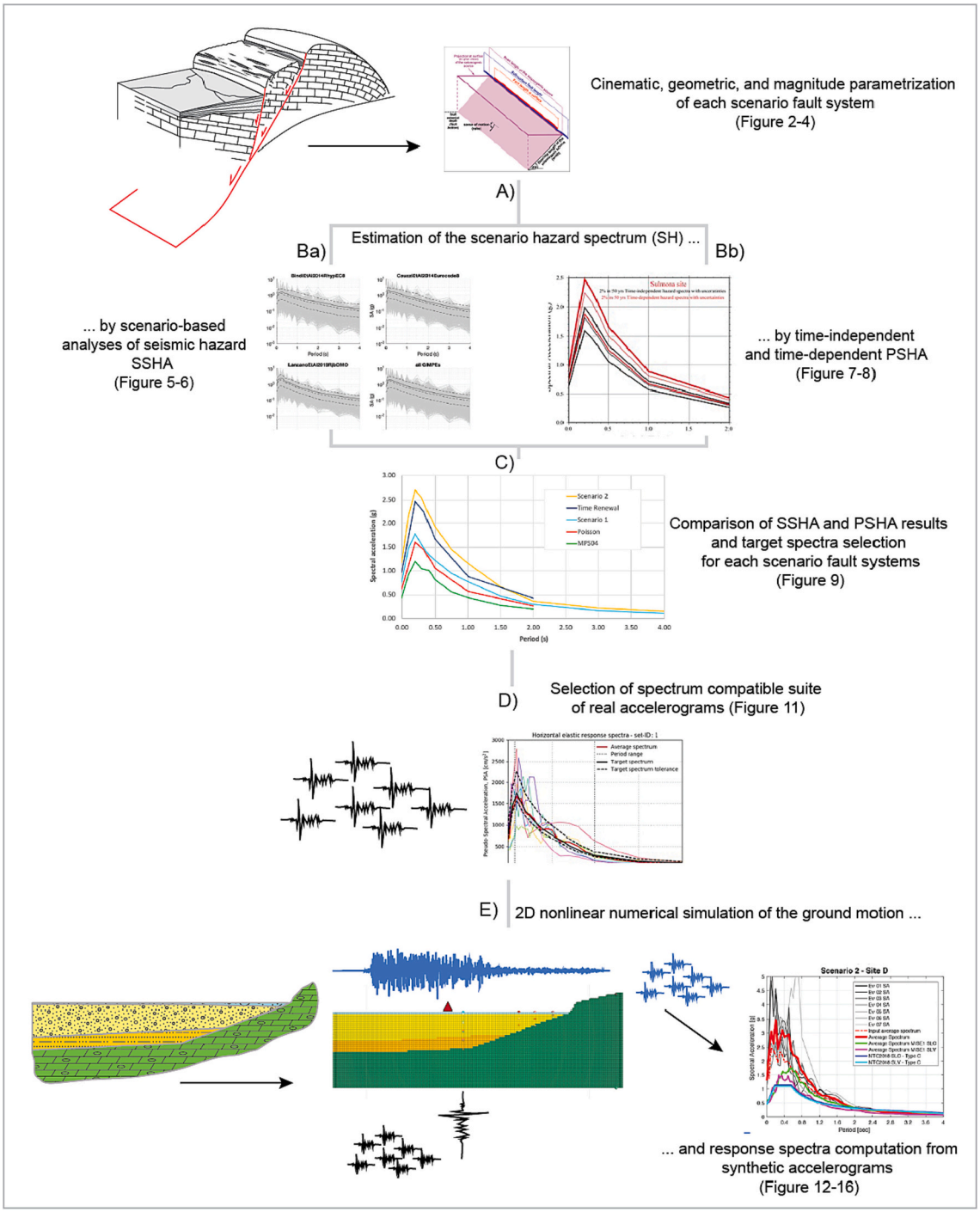

Fig. 1. Methodological flowchart implemented twice, for each fault scenario: A) Kinematic, geometric and magnitude parametrization of the fault system (see Figs. 2 and 4); B) Computation of the Seismic hazard (SH) spectrum by a) SSHA (Fig. 5-6) and b) time-independent and time-dependent PSHA (Fig. 7-8); C) Comparison of SH results and selection of target spectra for each scenario (Fig. 9); D) Selection of spectrum compatible suite of real accelerograms for each scenario (Fig. 11); E) 2D nonlinear numerical simulation of the ground motion using and average response spectra computation from synthetic accelerograms for each scenario (Fig. 15–17).

kilometers and thousands of kilometers (Iervolino et al., 2021, Al Shawa et al., 2021; Petricca et al., 2021), it is of engineering relevance to implement a methodology to account for the seismic input at the bedrock in the near fault areas. Further explanations of the biased prediction may be found in the low accuracy of current ground motion prediction equations (either Ground Motion Prediction Equations GMPEs, or Ground Motion Models, GMMs) at short distance from the fault, due to the lack of strong motion records located in near-source condition (Meletti et al., 2016; Sgobba et al., 2021a).

For sites located on soft sediment layers due to the high level of ground shaking expected in a near-source site, the nonlinear dynamic behavior of the soil is expected to be triggered by the coupling of the large magnitude and a short fault distance and it needs to be properly accounted for by numerical modeling methods. Though the Equivalent Linear method (EL) is widely used to solve dynamic problems, it can fail to provide conservative results when medium to large strains are reached during earthquake cycling loading. In these cases, to prevent excess damping and the consequent reduction of acceleration values, fully nonlinear methods need to be used.

This paper presents the application to a case study area in central Italy of a novel and non-standard approach to GRA, more specifically a scenario-based seismic hazard (SSHA) and PSHA analysis (Faccioli, 2006; Akinci et al., 2009; Akinci et al., 2017; Gerstenberger et al., 2020 and references therein) are implemented and compared to select the site-specific input motion and nonlinear GRA is performed.

The adopted and proposed comprehensive methodology (Fig. 1) takes into account several key-aspects:

i) geometric, kinematic and magnitude parametrization of the major active faults near the site;

ii) definition of the target response spectra based on a deterministic scenario-based analysis and comparison with both a time-dependent and time-independent probabilistic approach;

iii) selection of (bedrock) input accelerograms to be spectrum-compatible with the target spectrum;

iv) development of non-linear numerical modeling of the soil response to derive ground surface motions.

Since a comprehensive framework and roadmap for the near-fault areas is not yet available in design codes and standards, the procedure explained in this paper, with the implementation on a real case-study example of a complex site, can hopefully represent a useful model for the engineering and research community in the future as well as for various stakeholders involved in the delicate decision-making process associated with seismic risk reduction.

2. Case study characteristics

The investigated site, Case Pente (hereinafter referred to as CP), is in the Abruzzi region (Central Apennines), one of the highest seismic hazard regions of Italy (e.g.: Akinci et al., 2009; Petricca et al., 2015 and references therein). It lies at the SW edge of the Sulmona basin, (Fig. 2) a Quaternary hanging wall depression whose evolution is controlled by the Mt. Morrone normal fault system (MMF hereinafter) (e.g. Vittori et al., 1995; Miccadei et al., 1998; Gori et al., 2007, 2011), a seismogenic tectonic structure capable of releasing destructive earthquakes (M_W 6–7; e.g. DISS Working Group, 2021; Gori et al., 2011; Villani et al., 2014). The MMF bounds the basin to the NE and its trace in outcrop is roughly 4 km away from the CP site (Fig. 3 and Fig. 12). Such distance turns to zero using the Joyner-Boore definition of source-to-site distance (Kaklamanos et al., 2011).

The basin is filled with a sequence of slow velocity Quaternary continental deposits (Di Giulio et al., 2016; Rinaldini et al., 2007) of lacustrine, fluvial, and alluvial origin with lithologies spanning from

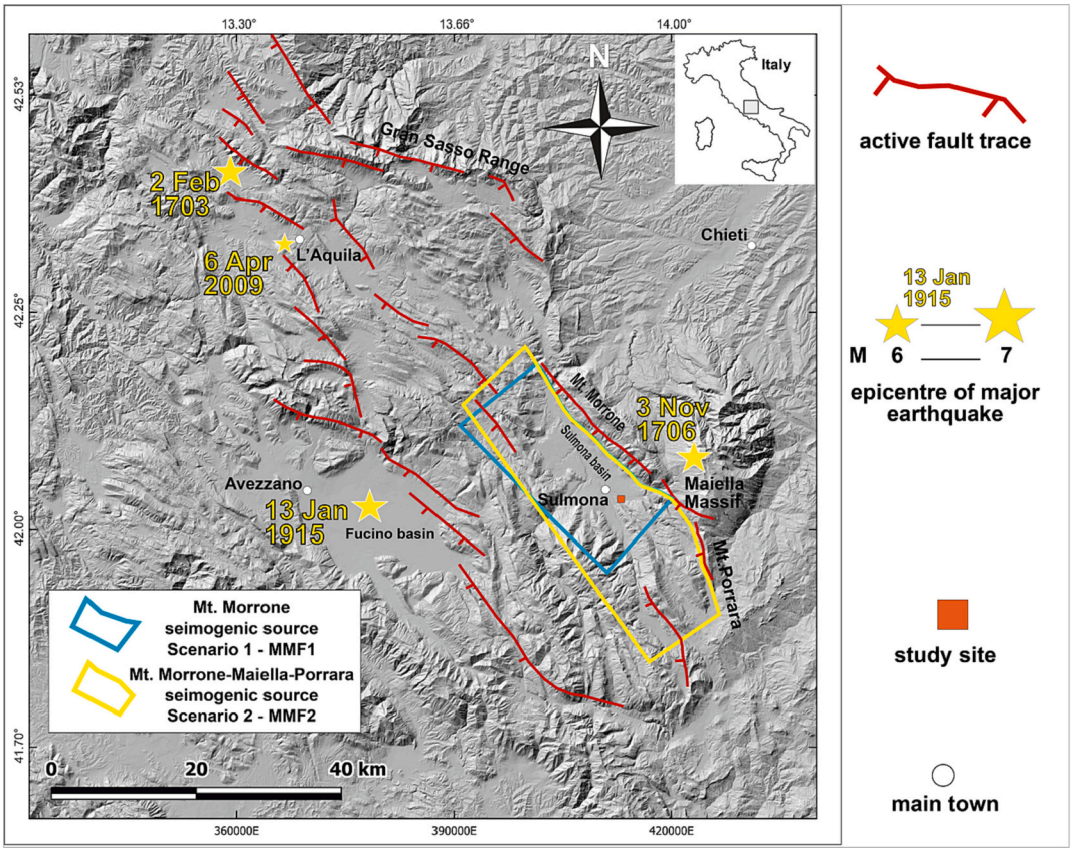

Fig. 2. Digital terrain model of the central Apennines with the trace of the major active normal faults (from Galadini and Galli, 2000; Gori, 2010; Falcucci et al., 2015). The surface projection of the two seismogenic sources scenarios (MMF1-MMF2) are shown using colored polygons.

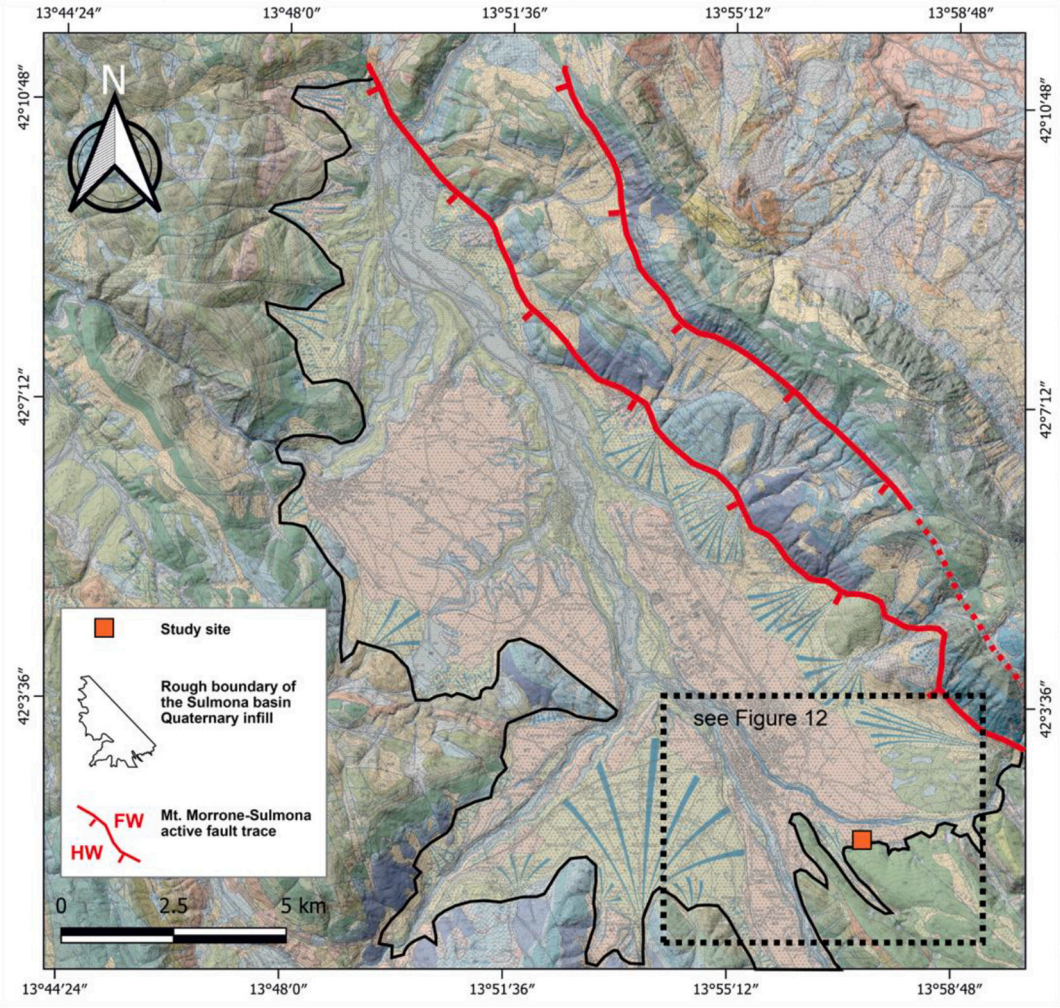

Fig. 3. Excerpt of the "Foglio 369 Sulmona" of geological map of Italy, 1:50.000 scale.

silts to sand and gravel. Though its maximum thickness is estimated at about ~450 m (e.g. Miccadei et al., 1998, 2002; Giaccio et al., 2009), at CP the bedrock is much shallower with lateral heterogeneities because of the valley border. In the area, important seismic amplification effects are reported by research studies (Di Giulio et al., 2016; Rinaldini et al., 2007; Yelikaya and Mercanlig, 2020; Villani et al., 2014) as well as by seismic microzonation studies (https://protezionecivile.regione.abruzzo.it/index.php/microzonazione). Also, relevant non-linear effects are expected at the site, due to coupling of important strains (triggered by large magnitude events at short fault distances) and loose granular deposits and cannot be accounted for using the soil class category approach.

This research work was developed between 2018 and 2019, addressing a request of the Italian Ministry of the Economic Development (formerly MISE, now Ministry of environment and energetic safety, MASE) through the General Division for the infrastructures and the safety of energy and geomining systems (DGISSEG), to develop and provide site-specific ground motion actions to be adopted in the performance-based design of an industrial facility planned to be constructed, taking into account the most prudent shaking scenario.

3. Geological framework

3.1. Seismotectonic background

The central Apennine chain has been affected by extensional tectonics since the Late Pliocene-early Quaternary, after the preceding compressive tectonic phase responsible for folding and thrusting of Meso-Cenozoic carbonate and Miocene-Pliocene foredeep basin terrigenous marine sedimentary sequences (e.g. Cosentino et al., 2010; Carminati and Doglioni, 2012). Quaternary tectonic extension led to the nucleation of normal fault systems mostly currently active, consisting of outcropping segments up to ~10–20 km long each, oriented NW-SE and dipping towards the SW (e.g. Galadini and Galli, 2000; Boncio et al., 2004; Galli et al., 2008) (Fig. 2). The long-term activity of the normal fault systems drove the formation of half-graben intermontane basins, in which hundred of meters thick continental sedimentary sequences accumulated (e.g. Bosi et al., 2003). The Sulmona basin, where the site under investigation is located, is one of these tectonic depressions that host lake, alluvial and slope deposits spanning the whole Quaternary (e.g. Miccadei et al., 1998; Giaccio et al., 2009; Giaccio et al., 2012). The major historical and instrumental seismicity of the central Apennines is commonly attributed to the activation of the active normal fault systems, responsible for large magnitude (up to 7) historical and instrumental seismic events (e.g. Akinci et al., 2009). Example are the 1915 M_W7 Avezzano earthquake, generated by the normal fault system affecting the Fucino basin to the NE (e.g. Galadini and Galli, 1999), and the 2009 M_W 6.3 L'Aquila earthquake, caused by the activation of the Paganica fault, located just E of L'Aquila (e.g. Falcucci et al., 2009; Emergeo Working group, 2010) (Fig. 2). The interaction of normal faults and Quaternary depositional/erosional processes allowed the analysis of the kinematic history of the extensional structures and to derive

kinematic parameters that describe their behavior and, hence, that of the associated seismogenic sources.

(https://www.isprambiente.gov.it/Media/carg/369_SULMONA/Foglio.html)

The Sulmona basin is one of the largest intermontane depressions of the central Apennines, showing about a NW-SE elongation, roughly 20 km long and up to 8 km wide (Fig. 2-3). The basin is surrounded by reliefs made of Meso-Cenozoic marine carbonate sequences and it includes since the Early Pleistocene up to about 400–500 m thick continental sedimentary sequence (e.g. Miccadei et al., 1998; Gori et al., 2014; Note Illustrative Carta Geologica d'Italia CARG, Foglio 369 Sulmona https://www.isprambiente.gov.it/Media/carg/369_SULMONA/Foglio.html) (Fig. 3). The area under investigation occurs at the southernmost sector of the basin, on top of an alluvial terrace carved on late Middle Pleistocene deposits ("Catignano Syntheme", Carta Geologica d'Italia Foglio 369 Sulmona https://www.isprambiente.gov.it/Media/carg/369_SULMONA/Foglio.html), near Colle Scipione, a carbonate relief on the south and the left flank of the Vella river (Fig. 3).

The SW slope of Mt. Morrone bounds the Sulmona basin to the NE (Fig. 2-3). This flank of the relief is affected by a NW-trending and SW dipping major normal fault (e.g. Vittori et al., 1995; Miccadei et al., 1998; Gori et al., 2007, 2011), known as Mt. Morrone (or Sulmona) normal fault (henceforth MMF). The scientific literature agrees in defining it as currently active and seismogenic. The fault consists of two major parallel splays, which are the shallow branches of the same seismogenic fault system at depth (Gori et al., 2011, 2014; Galli et al., 2015) (Fig. 4b). The fault displaced the continental deposits hosted in the basin, allowing geological recording of the recent kinematic slip history of the structure. Moreover, paleoseismological (Galli et al., 2015) and archaeo-seismological studies (Galadini and Galli, 2001; Ceccaroni et al., 2009) attributed to the fault an activation episode – likely to be the most recent one – occurred about two thousand years ago. This fact, together with the 1000–2000 years mean recurrence interval of the central Apennine major faults activation (e.g. Galli et al., 2008), defines

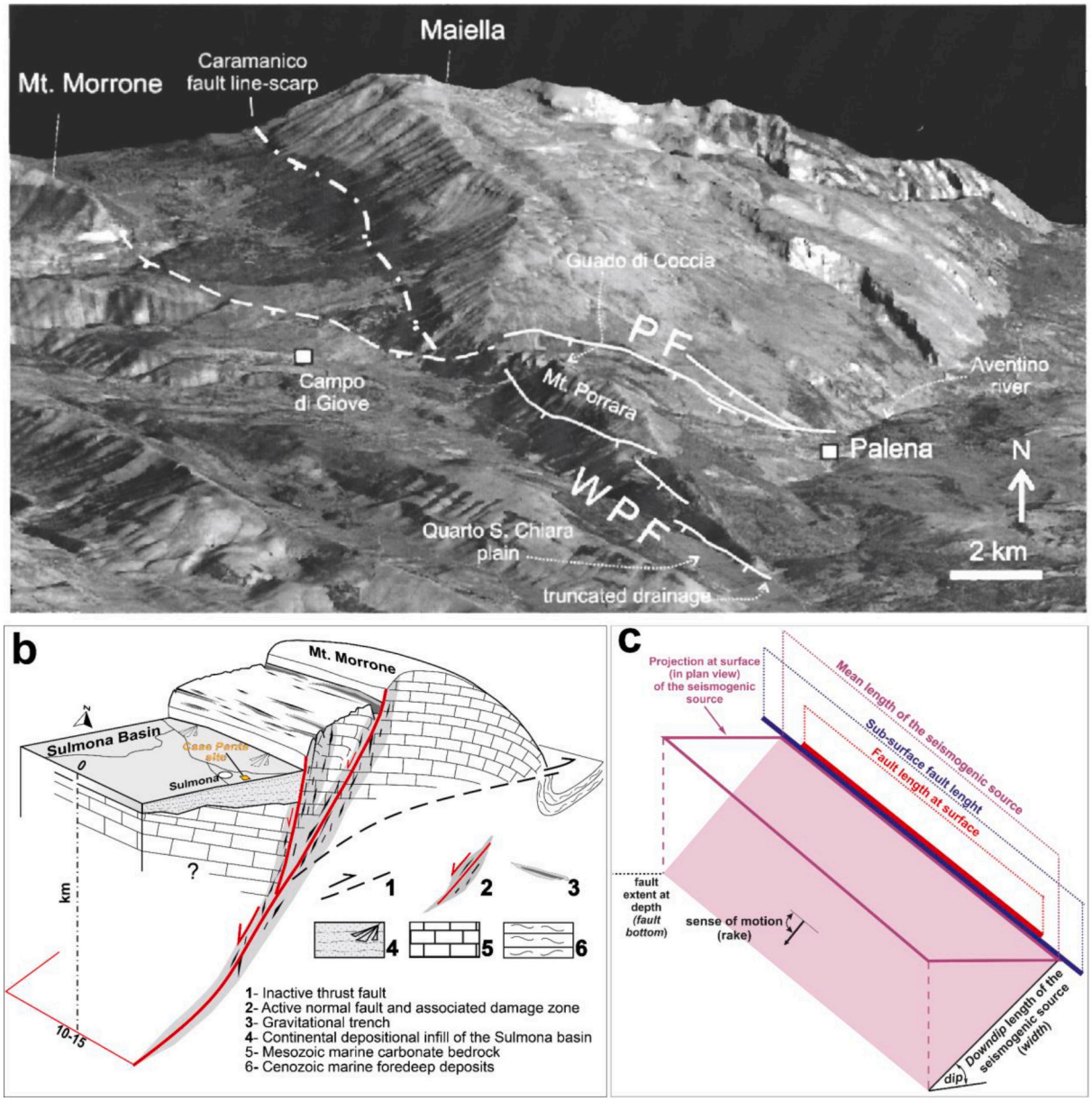

Fig. 4. a) Morrone Fault extension to Mt. Maiella and Mt. Porrara and other details; b) Block diagram of the structural setting of Mt. Morrone and of the Mt. Morrone-Sulmona seismogenic fault (modified from Gori et al., 2014), c) three-dimensional scheme of the seismogenic source model adopted in the present work (derived from Falcucci et al., 2018) and related geometric parameters.

the MMF as one of the most problematic seismic gaps of the central Apennines.

Just SE of the MMF, normal fault splays affect the southern sector of the Maiella Massif and the SW flank of Mt. Porrara (Fig. 2 and Fig. 4). These structures have been recently investigated (e.g. Gori, 2010; Pizzi et al., 2010; Patacca et al., 2021) and defined as the active Maiella-Porrara normal fault system (henceforth MPF).

Despite evidence of Late Pleistocene-Holocene activity, and probably during historical times, the role of MPF in the local seismotectonic framework is currently undefined. In this perspective, it is noteworthy that the area located between the Mt. Morrone, the Maiella Massif and Mt. Porrara has been the focus of one of the largest seismic events that struck the region over the past millennium, that is, the M_W 6.8, 1706 earthquake (Rovida et al., 2021). It caused severe damage to towns and villages over a vast area, reaching maximum intensity (MCS scale) I_0 10. The seismogenic source of the 1706 earthquake is still undefined and it thus remains one of the major open seismotectonic issues of the central Apennine chain. A few hypotheses have been recently proposed on the possible source of this seismic event: the activation of a blind thrust underneath the Maiella Massif (Lavecchia and de Nardis, 2010) or the activation of a blind back thrust of the Maiella Massif main thrust (Galli and Pallone, 2019). However, these hypotheses are only based on the distribution of the intensity datapoint related to the earthquake, and they lack any geological evidence of activity of the supposed causative reverse structures. Conversely, Gori (2010) hypothesized that the MPF had played a role in the seismogenic process that determined the earthquake, based on the geological evidence of historical activation of the structure and the dominant extensional tectonic setting of the region.

The bulk of the geological, geophysical, and seismological data allow us to make conceivable inferences on the geometric and kinematic characteristics of the seismogenic source related to the MMF. It deserves to be underlined that other major seismogenic sources are located within about 50 km from the Sulmona basin, as the Fucino fault (e.g. Galadini and Galli, 1999) and the Middle Aterno River Valley-Subequana Valley fault system (e.g. Falcucci et al., 2015), occurring W and NW of the Sulmona basin, respectively. Nonetheless, owing to its location and geometry, the MMF can be considered as the principal tectonic structure that determines the most severe ground shaking in the Sulmona basin and hence to the site under investigation. Therefore, we consider the MMF to explore the maximum possible ground motion scenarios in the basin.

3.1.1. Geometric characteristics

As for the geometry (Table 1), the ~22–23 km-long fault trace (e.g. Gori et al., 2011) strikes at around 145° (mean value) and at the surface, the main fault splays dip about 60°-70° SW-ward (e.g. Miccadei et al., 1998; Gori et al., 2011). Nonetheless, as seen in the recent seismic sequences of central Italy of 2009 and 2016–2017, generated by normal faults having the same geomorphic and structural surface features of the MMF, the mean dip angle of the whole fault may decrease downdip, reaching about 40°-45° along its deepest portion (e.g. Valoroso et al., 2013; Cheloni et al., 2014; Cheloni et al., 2019). This is also in agreement with other extensional seismotectonic frameworks, for example in Greece, where seismogenic normal faults and normal faulting earthquakes occur on fault planes, often with a listric shape, dipping in the range 35°-65° (e.g. Meyer et al., 1996; Koukouvelas, 1998). According to Doglioni et al. (2015), the dip angle influences the magnitude expected from a given normal fault, steeper normal faults generating higher magnitudes. Hence, 40°-60° dip values can be therefore assumed also for the MMF. In terms of extent at depth of the fault, seismological and geodetic data recorded during the 2009 and 2016–2017 seismic sequences in the central Apennines describes that the major seismogenic normal faults in the central Apennines reach about 10–15 km depth in the brittle upper crust (e.g., Doglioni et al., 2011; Chiaraluce et al., 2017; ;, 2019; Improta et al., 2019). This seems to fit seismological data collected in the Sulmona area by Romano et al. (2013), who defined that the MMF reaches to about 10–15 km depth.

3.1.2. Kinematic characteristics

As for the kinematic parameters (Table 2), the rake, that describes the sense of motion of the fault, can be assumed to be around 90°, that is, roughly dip slip (e.g. Gori et al., 2007, 2011). A small amount (10°-20°) – and thus negligible – of oblique component of the slip cannot be completely ruled out (e.g. Pizzi and Pugliese, 2004; Gori et al., 2011). The displacement of continental sequences and morphological features spanning the whole Quaternary allows us to assume a 0.4 ± 0.07–0.8 ± 0.09 mm/yr slip rate (e.g. Gori et al., 2007, 2011; Galli et al., 2015; Faure Walker et al., 2021). A vertical offset of about 1 m per event (at surface) can be derived from paleoseismological analyses performed in different places along the fault (Galli et al., 2015; Puliti et al., 2021). The observation made along the causative faults of the 2009 and 2016–2017 central Italy seismic sequences corroborates this estimate. In fact, the M_W 6.5 30th of October 2016 seismic event caused by the Mt. Vettore-Mt. Bove fault, which has an extent similar to the MMF, generated a mean vertical surface offset of about 1 m (up to about 1.8–2 m maximum vertical offset) all along the fault trace (e.g. Civico et al., 2018). In terms of fault activation history, the aforementioned paleoseismological and archaeo-seismological analysis defined that the last rupture of the whole structure probably occurred during the 2th century CE and the mean recurrence interval of fault activation in the range 2.4 ± 0.2 kyr, in agreement with the mean recurrence interval of the major active normal faults of the central Apennines.

3.1.3. Magnitude from rupture area

The above-described parameters allowed us to estimate the possible maximum rupture area of the MMF (Table 2) and, therefore, the maximum credible magnitude (**M**) of an earthquake generated by the structure. This value can be derived based on the regressions defined by

Table 2
Fault Parameters – Kinematics and Magnitude.

Fault	Rake (°)	Slip rate (mm/yr)	Slip (m)	Recurrence Interval (kyr)	Elapsed time (yr)	M 1	M 2
MMF1	−90	0.4 ± 0.07; 0.8 ± 0.09	1	2.4 ± 0.2	1800	6.6	6.7
MMF2	−90	0.4 ± 0.07; 0.8 ± 0.09	1	2.4 ± 0.2	1800	7	6.9

Table 1
Fault Parameters - Geometry.

Fault	Historic events	L 1 (km)	L 2 (km)	L (km)	Dip (°)	Strike (°)	Area (km)	Depth (km)	Dist (1)	Dist (2)	Dist (3)
MMF1	II AD	22.5	31	27	40–45	N145	505	10–15	0	13	3
MMF2	II AD	43	54	48	35–65	N145	860	10–15	0	11	3

(1) Joyner-Boore; (2) Hypocentre; (3) Fault rupture.

Wells and Coppersmith (1994) that relate the maximum expected magnitude with the fault length at surface or with the rupture area. The fault length was derived from fault trace mapping whereas the seismogenic fault rupture area was obtained according to the Falcucci et al. (2018) approach (Fig. 4c). Based on the foregoing, two plausible scenarios can be derived in terms of maximum rupture:

1. MMF rupture. This implies the complete rupture of the sole MMF, with rupture at surface of about 22–23 km; based on the mentioned Falcucci et al. (2018) approach, defines the rupture area of about 505 km^2 (Fig. 2). By applying the Wells and Coppersmith (1994)'s regressions, a maximum credible magnitude **M** 6.6–6.7 can be derived. Comparably, Valentini et al. (2017) proposed the "Sulmona" seismogenic fault associated with the MMF, being 20 km long at surface and 22.6 km long at depth, with associated **M** 6.5 ± 0.2.
2. MMF-MPF synchronous rupture. Owing to the proximity of the MPF to the MMF, a plausible scenario where the two structures rupture synchronously as a single seismogenic source must also be considered. This implies a 43 km total fault length at surface and a 806 km^2 maximum rupture area (Fig. 2-4). This yields around **M** 7 maximum credible magnitude. This estimate agrees with the M_W estimated for the aforementioned 1706 earthquake, which testifies to the occurrence of magnitude ~7 earthquakes in the Sulmona basin area. Also, the possible activation of the MMF with nearby active faults, potentially responsible for earthquakes with **M** ~ 7, has been recently hypothesized by Di Domenica and Pizzi (2017), based on speleoseismological data.

An alternative computation of the maximum magnitude can be obtained by calculating the hanging wall brittle volume that can be mobilized along the normal fault (Petricca et al., 2015), which is in the order of about 10.000–12.000 km^3 reaching a possible **M** 7–7.2.

In the Italian Database of Individual Seismogenic Sources (DISS) (http://diss.rm.ingv.it/diss/), an individual source (ITIS027) is associated with the MMF. The related **M** is slightly lower, i.e. **M** 6.4, then that defined in the present work and in many other articles; this is probably due to the assumption of a smaller seismogenic fault.

4. Site specific seismic hazard analyses

In the following section the seismic hazard in the case study area is assessed using both a deterministic scenario-based approach and a probabilistic approach.

4.1. Scenario-based approach

To assess the impact of the seismogenic potential of the MMF1 and MMF2 with the two selected magnitudes and the relative distance between them and the CP site (Table 1), a "Scenario-based" approach has been adopted, which consists in the calculation of ground motion from a single earthquake rupture scenario considering several empirical ground motion models (GMMs) with the associated aleatory variabilities.

According to the parametrization in Tables 1 and 2, the selected scenarios are:

- Mt. Morrone fault, Mw 6.7 (MMF1)
- Mt. Morrone fault-Maiella-Porrara, Mw 7.0 (MMF2)

For both cases, to be consistent with the tectonic and seismological knowledge of the area, a normal mechanism was assumed with the hypocenter of the rupture located in the center of the source, ~8 km deep. As regards the GMMs, we adopted the two models selected for the most recent hazard model for Italy (MPS19, Meletti et al., 2021), i.e. Bindi et al. (2014) and Cauzzi et al. (2015) and the updated version of the national GMM called ITA18 (Lanzano et al., 2019). In particular, the Bindi et al. (2014) and Cauzzi et al. (2015) models derive from a preselection of 16 candidate GMMs performed over nearly one thousand models published in literature adopted for active shallow crustal regions, performed by Lanzano et al. (2020), for the MPS19 project. These two GMMs provide estimates of ground shaking in terms of the geometric mean of the horizontal components for PGA and 5% damped spectral acceleration, $S_a(T)$, up to 4 s and 10s, respectively.

The third GMM selected by Lanzano et al. (2020) was the Bindi et al. (2011), however, in this work we adopted the last update of this GMM as proposed by Lanzano et al. (2019). It returns the median value of the geometric mean of the two horizontal components rotated through all nonredundant period-independent angles, for PGA and 5% damped $S_a(T)$ up to 10s.

The three GMMs are calibrated on different datasets: Bindi et al. (2014) used a Pan-European dataset, Cauzzi et al. (2015) a global dataset, and Lanzano et al. (2019) an Italian dataset.

Geometric and kinematics parameters described in the Section "3.2. The Mt. Morrone seismogenic source parameterization" served as input for the GMMs. Length, strike and dip, for which we used the central value of the range given in Table 1, are used to locate the three-dimensional geometry of both sources, MMF1 and MMF2, and to calculate the appropriate site-source distance (Kaklamanos et al., 2011).

The site-source distances used by the 3 GMMs are, respectively, hypocentral distance (Rhypo) for the Bindi et al. (2014), distance from the rupture (Rrup) for the Cauzzi et al. (2015), and Joyner-Boore (Rjb) distance for Lanzano et al. (2019).

Table 1 reports the distances in kilometers for the two sources considered for the case study, according to the aforementioned GMMs. The coefficients of the GMMs equations were coherently selected according to the faulting style (normal) and rigid soil (Soil Type A, according to the NTC2018 regulation).

A set of n- intensity measurements (with $n = 1000$) have been generated (PGA and 11 Sa(T) up to $T = 4$ s), randomly sampling the acceleration values within +/− 3 standard deviations from the median of each GMM. It is worth noting that the scenario-based approach does not need to determine the probability of occurrence of the specific rupture, it only needs sufficient information to parameterize the location and the geometry, the magnitude, and the style-of-faulting of the seismic source. In this way we were able to derive a statistical distribution of the shaking values with the corresponding percentiles.

Thus, for each group of ground shaking derived from a GMM, and for each $S_a(T)$, statistics relating to the 50^{th}, 84^{th}, 90^{th} and 97.5^{th} percentiles of the distribution were calculated. Moreover, we equally weighted the predictions of the 3 GMMs distributions to obtain the combined SSHA spectra. The results along with their statistics are shown in Fig. 5 and Fig. 6.

Given the importance of the site facilities and following a conservative (safety-side) approach, the 90% percentile of the distribution was selected as corresponding to approximately mean + 1.3 standard deviations and chosen as target spectrum at bedrock.

The two target spectra (Table 3) used for the subsequent analyses correspond to the combined spectra (Figs. 5 and 6) and hereinafter referred as Scenario spectra.

4.2. Probabilistic Seismic Hazard Analyses

The strategy followed in a traditional and currently adopted PSHA approach is based on the memoryless (time-independent) property of the Poisson processes where time, size, and location of previous events are all assumed to be independent. However, the time-varying (or time-dependent) event models have been increasingly used as part of PSHA in Italy (Akinci et al., 2009; 2017) and worldwide (Field et al., 2015). As part of the MISE DGISSEG agreement, the seismic hazard for this study was assessed using a time-dependent probabilistic approach. To this end the long-term probabilistic hazard was calculated considering the single faults as the 3-D geometry of the fault system, the geological slip rates of each individual fault, and the instrumental seismicity (Petersen et al.,

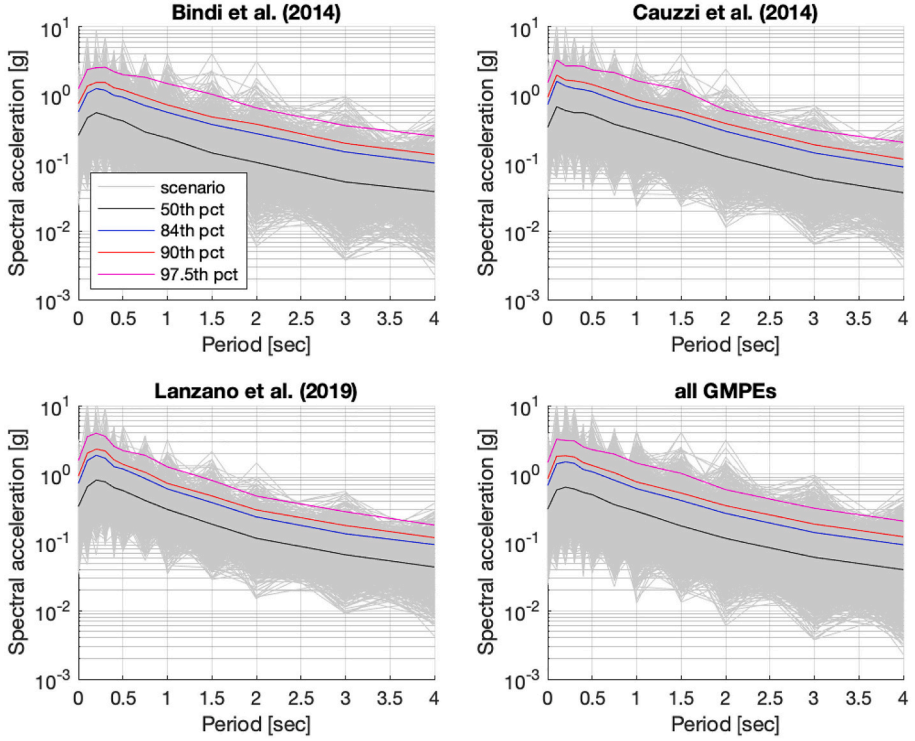

Fig. 5. Mt. Morrone Fault M_w6.7 (MMF1): envelopes of SSH Spectra and statistics relating to the 50th, 84th, 90th, 97.5th percentiles. The legend applies to all panels.

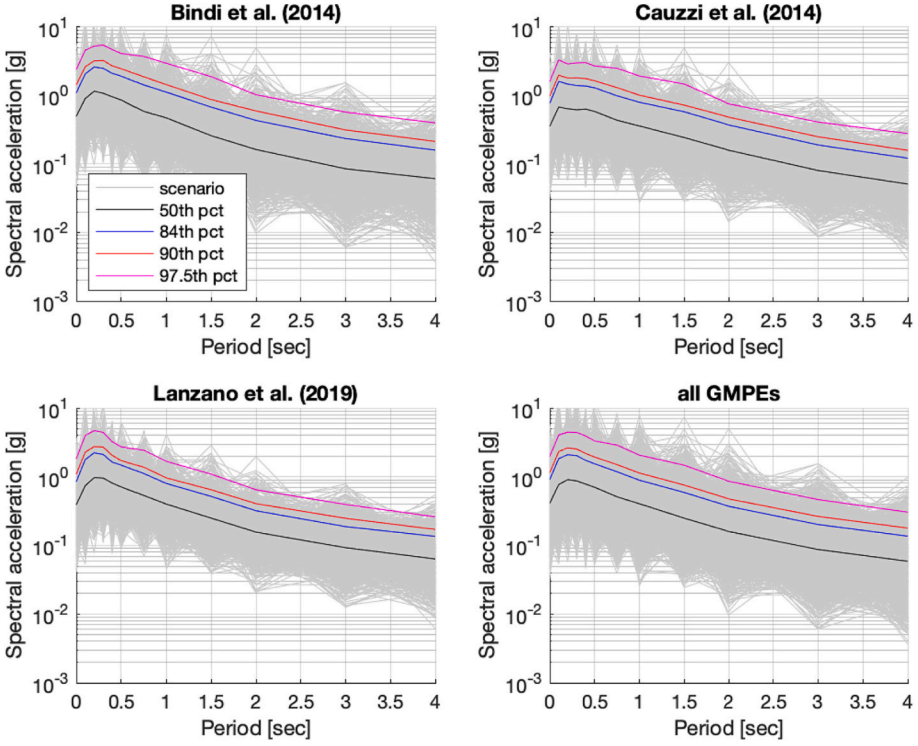

Fig. 6. Mt. Morrone Fault M_w7 (MMF2): envelopes of SSH Spectra and statistics relating to the 50th, 84th, 90th, 97.5th percentiles. The legend applies to all panels.

Table 3
Target spectra values.

Scenario	0 s	0.1 s	0.2 s	0.3 s	0.4 s	0.5 s	0.75 s	1 s	1.5 s	2 s	3 s	4 s
M_w 7 - MMF2	1.14	2.32	2.64	2.53	2.18	1.94	1.5	1.13	0.76	0.48	0.26	0.18
M_w 6.7 - MMF1	0.85	1.81	1.84	1.77	1.47	1.33	1.04	0.77	0.53	0.34	0.19	0.12

2014). The seismic hazard model constructed to assess the ground motion shaking describes the seismic potential of a region as the sum of two contributions:

1. The background seismicity, that is, the activity of small-to-moderate magnitude events not associated with well-known tectonics structure;
2. The fault-based source models describing long-term earthquake rates caused by individual fault ruptures (or well-defined fault segments).

These two seismicity models are integrated into a single model, using a logic tree approach.

4.2.1. Characterizing background seismicity

The calculation of the seismic potential from the background seismic activity (small magnitude events) is estimated using the adapted smoothed seismicity approach developed by Helmstetter et al. (2007) and applied for Italy by Akinci et al. (2018), based on a spatial smoothing of instrumental seismicity. The instrumental catalog used contains earthquakes recorded in 1981–2016 (Gasperini et al., 2013), with magnitude $6.5 \geq M_W \geq 1.0$ and magnitude completeness $M_{w \geq} 3.0$, as suggested by the same authors. The earthquake catalog is declustered using the method of Gardner and Knopoff (1974). The magnitude frequency distribution (MFD) between earthquake magnitude and recurrence rate is estimated using the Gutenberg and Richter truncated exponential model with the value of $b = 1.0$ and assumed homogeneity over the entire study area. A detailed description of the model applied to various regions in Italy is reported in Akinci et al. (2018) and references therein.

4.2.2. Modeling the fault sources

Regarding to fault-based source models, different geological structures were considered; the main structure near the Sulmona site, the MMF2 M_w7.0, presented in section 3, and other structures that can produce strong and moderate earthquakes, of magnitude $M_w \geq 6.0$, close to test site were adopted from Akinci et al. (2009). The return period, relative to each seismic source, was calculated through the assumption that the total seismic moment rate from the magnitude distribution equals the geological moment rate (Field et al., 1999) which can be estimated by $T_r = M_0 / (\mu \, \mathring{u} \, L \, W)$, where the seismic moment is given in terms of magnitude $M_0 = 10^{1.5Mmax+9.05}c$ the coefficient 9.05 (SI units) defined by Hanks and Kanamori (1979), but rounded to 9.0 by Anderson and Luco (1983), μ is the elastic shear modulus of the crust (a typical value is 30 GPa, 3.0×10^{10} N.m), $\mathring{u}$ is its slip rate, and L is the length of the fault, W is the downdip width of the fault. The main geometric and kinematic characteristics of Mt. Morrone fault for the Scenario 2 - MMF2, listed in Tables 1 and 2 are considered for the calculations.

4.2.3. Calculation of time-independent and time-dependent probability in seismic hazard analysis

Both the (time-independent) Poisson and the (time-dependent) Brownian Passage Time (BPT) renewal models were adopted to estimate the probability of an earthquake occurrence for each fault segment of the MMF2. Contrary to the Poisson model, the time-dependent renewal process reflects the expectation that, after an earthquake occurs on a fault section, another rupture can occur on the same fault section after sufficient time has passed to re-accumulate the stress (Ellsworth, 1995; Ogata, 1999). This model requires at least two parameters and usually includes knowledge of the time of the most recent rupture, T_e. The two parameters are: i) the recurrence rate of events, T_r. and ii) aperiodicity, α, which is a measure of the irregularity of the length of the time interval between consecutive events. In this study, because of the limited number of historical events observed at each individual fault, the aperiodicity parameter $\alpha = 0.5$ was selected as the provisional generic value as recommended by Ellsworth et al. (1999).

In Fig. 7, the future earthquake occurrence probability on the MMF2

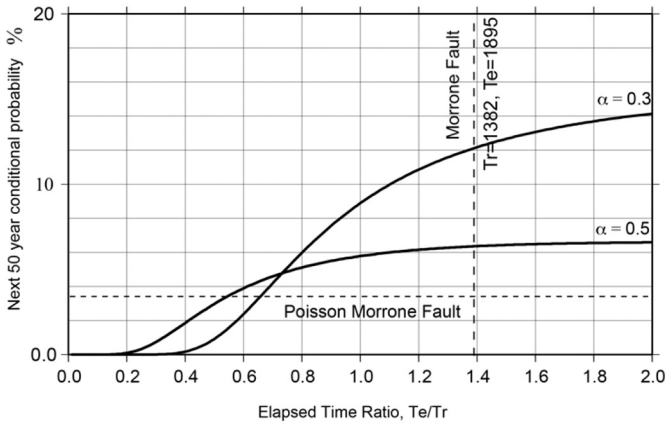

Fig. 7. The 50-year probability of earthquake occurrence on the MMF2 as a function of elapsed time, providing a 1382-years return period calculated from maximum slip rate, was determined using (time-dependent) Brownian Passage Time and (time-dependent) Poisson models for recurrence. α is the aperiodicity parameter utilized to represent the dispersion in the density function.

is presented based on both the time-dependent and time-independent models. For the latter calculated as an effective Poisson rate with two different aperiodicity values, namely 0.3 and 0.5, has been adopted. The MMF2 leads to higher probability from the BPT model, and the occurrence probability for the next 50 years strongly increases with the elapsed time ratio when compared to the Poisson. The elapsed time of 1895 years is in fact well beyond the return period of 1382 years from the maximum slip rate. Its elapsed time ratio, defined as the ratio of the time since the last earthquake, and the mean recurrence time of the earthquake, is 1895/1382 = 1.37, thus larger than the 1.0, meaning that a major earthquake event should be considered "overdue". For the MMF2 scenario, the BPT approximation leads to a 13% and a 7.5% probability of occurrence within a 50-year period for $\alpha = 0.3$ $\alpha = 0.5$ respectively. The BPT 50-year probability for $\alpha = 0.3$ and 0.5 builds-up right after the last event and it becomes larger than the Poisson probability, when the time passed from the last earthquake is long past approximately two-thirds of the mean recurrence time. The Poisson probability for the same fault is 3.6% thus much smaller than the BPT renewal models.

4.2.4. Probabilistic seismic hazard calculations

The Poisson and BPT models together with the geological slip rate parameters (Table 1-2), were used to calculate the variability of the seismic hazard (Akinci et al., 2010) following the maximum characteristic earthquake assumption. The regional attenuation relationship derived by Malagnini and Herrman (2000) and Malagnini et al. (2011) and applied for the MPS04 official seismic hazard maps is adopted as a predictive model of ground motion for the study area (Montaldo et al., 2005). The results of the seismic hazard analysis are presented in terms of $S_a(T)$ at the five structural (equivalent Single Degree of Freedom Oscillator, SDOF) periods ($T = 0.2$ s, 0.3 s, 0.5 s, 1.0 s, and 2 s), with a 2% probability of exceeding in 50 years (corresponding to a return periods of 2475 years) and with the hazard curves calculated using both Poisson and renewal probabilities determined from the three different slip rate values (minimum, average, maximum values as given in Table 1-2).

The uncertainties on the slip rate, which may cause variations in the recurrence parameters, were taken into consideration for the seismic hazard analysis (Akinci et al., 2010). The calculated response spectra and hazard curves at the Sulmona site are presented in Fig. 8a-b using both the Poissonian and renewal method.

It is worth highlighting that the time-dependent hazard curves as well as the $S_a(T)$ mostly and consistently present larger accelerations for the case study site when compared to the more traditional (code-based

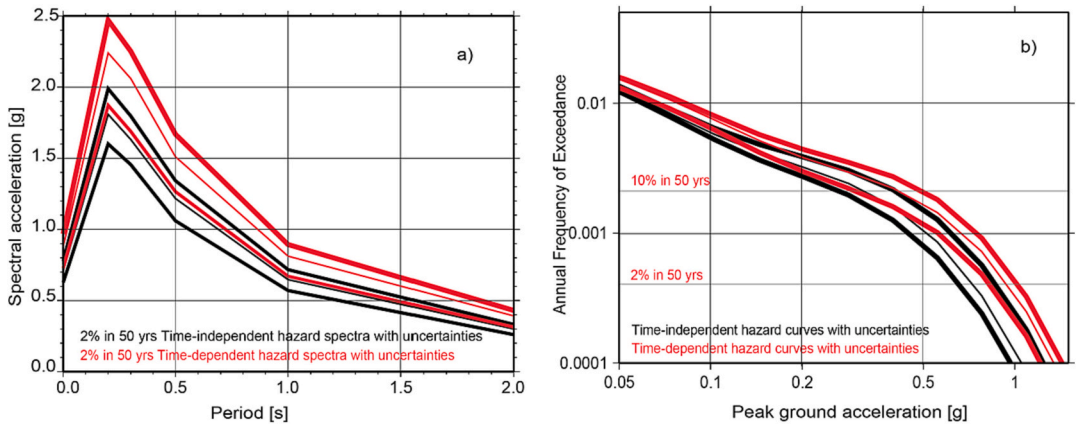

Fig. 8. a) Spectral response accelerations at return periods of 2475 years for the CP site obtained using both the Poissonian model (black line) and the renewal (BPT, red line) with the maximum, medium and minimum slip rate (thick and thin lines, respectively) representative of a part of the uncertainty on the hazard, b) Hazard curves for the Sulmona site obtained using both the Poissonian model (black line) and the renewal (BPT, red line) with the maximum and minimum slip rate (thick lines), and average slip rate (thin lines). The horizontal lines represent the 10% and 2% probability of exceedance in 50 years, respectively. The ordinate shows the annual frequency of exceedance values and the peak horizontal acceleration values (PGA)in g. (For interpretation of the references to colour in this figure legend, the reader is referred to the web version of this article.)

PSHA) and time-independent Poissonian approach. In fact, the probability of occurrence of the MMF2 Scenario, evaluated by the BPT renewal model, exceeds the Poissonian one. MMF2 has a longer elapsed time when compared to its recurrence time, therefore with the renewal BPT model it has a higher probability of occurrence than that obtained by the Poisson model. The maximum PGA value obtained from the time-dependent BPT model is around 0.97 g and exceeds the value of 0.77 g (at about T = 0.2 s) calculated with the Poisson model with a 2% probability of exceedance in 50 years (corresponding to a return period of 2475 years).

4.3. *Selecting the target spectrum*

Fig. 9 presents the comparisons between the hazard spectra

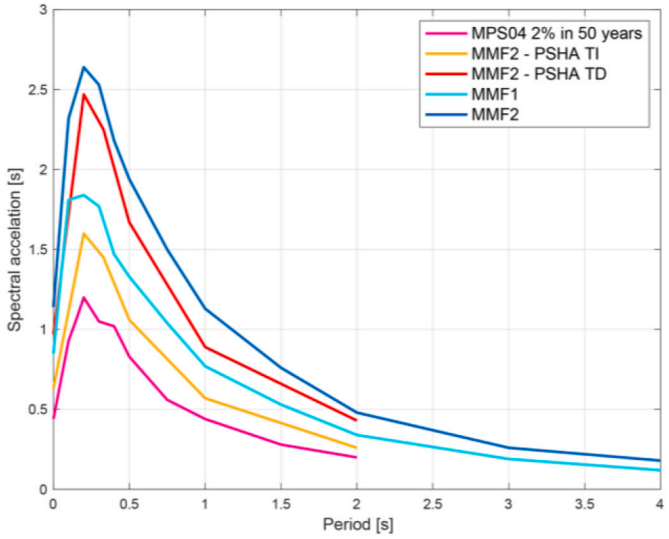

Fig. 9. Comparison among hazard spectra obtained by deterministic approach from Scenario 1–2 (MMF1, M_w6.7 and MMF2, M_w7.0) equal to the 90th percentile of the statistical distribution), probabilistic approach for Scenario 2 with renewal (with maximum slip rate) and Poisson (with minimum slip rate) models for 2% probability of exceedance in 50 years (for a return period of 2475 years) and the MPS04 model for a probability of exceeding 2% in 50 years (http://esse1-gis.mi.ingv.it/) used in the 2018 NTC regulation to obtain the normalized spectrum for the state limit of collapse prevention (SLC).

computed following two different approaches, namely: a) a probabilistic approach, either based on a time-independent Poisson model and a time-renewal or BPT model for a 2% probability of exceedance in 50 years; b) a "Scenario-based" process; and c) the MPS04 model (Montaldo et al., 2007) for a 2% probability of exceedance in 50 years, representing the normalized spectrum for the Collapse Prevention limit state (SLC) in the NTC2018, Norme Tecniche per le Costruzioni, 2018.

Note that according to the NTC2018 the return period corresponding to a 5% probability of exceedance in 200 years would be 3899 (SLC), but a cap (upper bound) value of 2475 is prescribed to be used by the same NTC2018 document. Therefore the 2475 return period uniform hazard spectra (UHS) should in principle be used to represent the NTC2018 code-based approach.

The comparison between the two approaches shows that the SSHA for Scenario 1 (Mt. Morrone M_w6.7, MMF1), is comparable for Scenario 2 (Mt. Morrone M_w7.0, MMF2) with that predicted by using the minimum slip rate and the time-independent Poisson model for a return period of 2475 years (see Table 4). Moreover, the SSHA for Scenario 2, provides comparable results with the curve obtained using the maximum slip rate and the time-dependent/renewal BPT model for a return period of 2475 years (see Table 4). Fig. 10 also presents a detailed comparison between the two approaches (probabilistic vs. scenario-based) in terms of hazard curves that have highlighted that the PGA values derived with the scenario-based approach for the Scenario 2 - MMF2 Morrone (M 7.0) are comparable with those derived with a time-dependent Poisson approach. Assuming an Importance Level IV (Use Class IV according to the NTC2018, leading to a Use Coefficient Cu = 2.0), and a nominal life of the facility Vn =100 years, thus a reference period Vr = CuVn = 200 years, the hazard curves associated with the key limit states, namely period Vr = CuVn = 200 years, the hazard curves associated with the key limit states, namely Operational (SLO), Damage Control (SLD), Life Safety (SLV) and Collapse Prevention (SLC), are derived and provided, for various percentiles of the distributions, as derived from the three GMMs for the MMF2 Mt. Morrone (M 7.0) fault-

Table 4
S_a (T) minimum (Poissonian from the minimum slip rate, TI) and maximum (renewal model from the maximum slip rate, TD) values expressed in g for a return period of 2475 years.

Model	S_a(T)	0 s	0.2 s	0.33 s	0.5 s	1.0 s	2.0 s
TD	Max.	0.97	2.47	2.25	1.67	0.89	0.43
TI	Min.	0.63	1.60	1.45	1.06	0.57	0.26

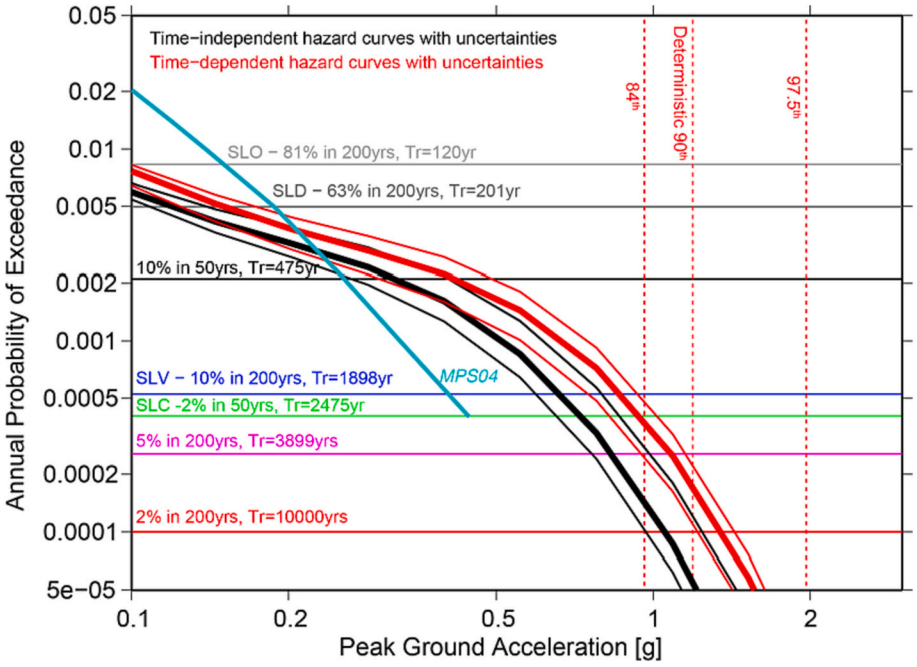

Fig. 10. Hazard curves for the Sulmona site were obtained using both the Poissonian model (black line) and the renewal (BPT, red line) with the maximum and minimum slip rate (thick lines), and average slip rate (thin lines). The ordinate shows the annual frequency of exceedance values and the peak horizontal acceleration values (PGA) in g. The horizontal reference lines represent 10%, 5%, and 2% probability of exceedance in 50 and 200 years, respectively. The demand curves associated with the e limit states SLO (Operational), SLD (Damage Control), SLV (Life safety), and SLC (Collapse Prevention), are calculated assuming Importance Level (Class of Use) IV, thus Coefficient of Use Cu = 2.0, Nominal life Vn = 100, leading to reference period Vr = 200 years. The vertical reference lines show the ground shaking values in terms of PGA corresponding to the 84^{th,} 90th, and 97.5th percentile of the distributions obtained using the three predictive ground motion models, GMM for the MMF2 Mt. Morrone fault based deterministic scenario. (For interpretation of the references to colour in this figure legend, the reader is referred to the web version of this article.)

based deterministic scenario.

More specifically, the time-dependent probabilistic hazard curves, corresponding to either 5% and 2% of annual probability of exceedance in 200 years, provide a range of PGA values, respectively, from about 0.9 g to 1.1 g and from about 1.1 g to 1.3 g in the uncertainty range of the slip rate. The SSHA scenario at the 90th percentile provides similar values in agreement with the PGA associated with the 5% probability of exceedance in 200 years.

Overall, considering that the 84th and 97.5th percentiles represent the mean + 2 and 3 sigma (standard deviation) scenario of the shaking level, assuming a 90th percentile curve derived with a deterministic MMF2 Scenario 2 approach for design purposes would represent a reasonably precautionary estimate of the criticality of the expected ground motion and would well agree with the PGA values derived from a probabilistic time-dependent approach.

5. Seismic input selection

To select the set of acceleration waveforms to be used as input for the ground response analysis, a methodological approach widely established in engineering practice was implemented, as prescribed by several seismic codes worldwide, including NTC18 and Eurocode 8. In line with these provisions, the accelerograms for dynamic analysis can be chosen from natural (i.e., actually recorded), artificial (i.e., obtained by applying random vibration theory) or generated using physics-based simulation models. However, the increasing availability of real records of ground motion in worldwide archives has shifted the community's attention primarily towards the use of natural accelerograms (e.g., Bommer and Acevedo, 2004). The latter are considered to be inherently more realistic in terms of frequency content, duration, number of cycles, and correlation between horizontal and vertical components of seismic motion, although a condition for their reliable use is that they conform to the seismic scenario and hazard conditions of the site under consideration. This aspect implies that the *average* response spectrum of the selected accelerograms of a given combination must be compatible with the target design spectrum within the assigned tolerances and period limits (a condition also known as "spectral compatibility" or "spectral matching").

Grounding on this approach, the seismic input signals for the subsequent nonlinear soil modeling were selected among large record databases using the REXELweb code (Iervolino et al., 2010; Iervolino et al., 2011; Sgobba et al., 2019, 2021a), to be compatible with the 90th percentile of the enveloping spectra for the scenarios MMF1 and MMF2 which were assumed as the target.

More specifically, the suite of accelerograms in REXELweb draws from the following accredited datasets: (i) ESM (Engineering Strong Motion Database, https://esm-db.eu/; Luzi et al., 2020), which contains accelerograms registered in Europe and in the Middle East countries for events of magnitude greater M4; (ii) ITACA v.3.1 (Italian Accelerometric Archive, http://itaca.mi.ingv.it; D'Amico et al., 2020) that is the archive of accelerometric data recorded in Italy from 1972 until 2018 related to earthquakes with magnitude M > 3.0 and containing more stations metadata for Italy compared to ESM and iii) NESS2 (the NEar Source Strong-motion dataset, http://ness.mi.ingv.it/; Sgobba et al., 2021b), in order to specifically include near-fault ground motions recorded worldwide in the selections. The time-history acceleration signals stored in these repositories are all processed homogeneously, through a manual procedure (Puglia et al., 2018) and associated with event and station metadata updated periodically. The entire workflow was built upon the methodology described by Sgobba et al. (2019, 2021a), refer to this for further details.

Additional selection constraints were set as follows:

- Minimum/maximum magnitude for MMF1: 6.4–7.0 (i.e. the scenario magnitude M_w 6.7 ± 0.3).
- Minimum/maximum magnitude for MMF2: 6.6–7.4 (i.e. the scenario magnitude M_w 7.0 ± 0.4; note that for this scenario it was necessary to broaden the magnitude range, with a tolerance of ±0.4 around the mean value, due to the paucity of records from strong earthquakes).
- Minimum/maximum epicentral distance R_{epi}: 0–20 km.
- Both analog and digital records were included.

We performed the matching analysis with minimal restrictive criteria so as not to limit the number of recordings obtained too much and to avoid applying scaling factors, which alter the amplitude of the original accelerogram and may introduce some potential biases in response modeling (Manfredi et al., 2022).

After setting the above options, the spectra were preliminary selected and ordered on the basis of a *score* index δ_j (for each j-th spectrum)

which is a synthetic measure (namely the root-mean-squared-error) of the distance between the target spectrum Sa_{target} and the spectrum of an individual record Sa_j over the N periods T_i of interest:

$$\delta_j = \sqrt{\frac{1}{N}\sum_{i=1}^{N}\left(\frac{Sa_j(T_i) - Sa_{target}(T_i)}{Sa_{target}(T_i)}\right)^2}$$

Compatibility with the target was identified by drawing from the list of pre-selected spectra according to the following criteria: i) match satisfied in the period interval between $T_{min} = 0.1$ s - $T_{max} = 2.0$ s (according to the natural vibration periods of the most common structural types in Italy); ii) tolerance above and below the target spectrum of 30% and 10%, respectively. The lower limit was slightly extended for the MMF2 scenario to 30% from that prescribed by NTC2018, in order to ensure at least one combination of records with an acceptable δj. In detail, we imposed a threshold value of $\delta j = 0.2$ as the maximum mean misfit between the *average* spectrum and the target to prevent the selection of records with a spectral shape too different from the target. Improved selections were finally obtained by visual checking and iterative exclusion of specific records associated with higher scores. On these bases, the best combinations of accelerograms with the smallest average score was identified, as reported in Table 5. The response spectra of two combinations are also presented in Fig. 11 and compared with the corresponding target spectra and tolerances. Among the 7 accelerograms for the scenario MMF1, 4 of them are related to the event of Mw 6.5 Norcia (central Italy) which occurred in 2016 and recorded at stations very close to the rupture fault, whereas two are related to Japanese events (Kumamoto, Mw7, of 2016 and Niigata Mw6.6, of 2004) and one to the Iranian earthquake of Bam, Mw7 occurred in 2003. Although the selection of Japanese and Iranian records may appear inconsistent with the case-study, the rationale applied here aimed to achieve spectral matching as a sufficient condition to ensure correct input estimation for site response analysis, making it de-facto unnecessary to force accelerograms to come from the same focal mechanism, seismic source or site conditions as the target spectrum. An implicit assumption underlying this consideration is that when considering similar tectonic regimes, as in the present case (we selected only active crustal events), strong-motion records from one country can be selected and applied in another country (Bommer and Acevedo, 2004).

Finally, some of the selected records are pulse-like, which is an important feature to include in the selected records as they are associated with a large velocity pulse and unusual response spectral shape amplified in a narrow frequency-band (Sgobba et al., 2021c). These impulses can cause an increased seismic demand to structures located near the fault rupture (Chioccarelli and Iervolino, 2010), therefore we found it important to include such an effect in the selection. The recordings of the scenario MMF2 are all related to Japanese events (Kumamoto, Mw7, 2016; Niigata-Ken-Chuetsun Mw6.6, 2004 and Iwate-Miyagi Nairiku, Mw6.9, 2008), due to the lack of high-quality records from Italian earthquakes at these high-magnitudes. Also, one waveform with impulsive shape (BO.KMM17.00.HN.USGSus20005iis) can be found in this set. A plot with all the selected waveforms can be found in the Appendix (Fig. S1-S2).

6. Ground response analyses

Dynamic two-dimensional numerical modeling of the local seismic response is a common tool used to predict the amplification effect at the surface at the scale of engineering sites, in seismic microzonation studies and research. Based on geological and geotechnical models of the subsoil and using appropriate calculation techniques, the propagation of seismic waves is simulated to obtain synthetic seismic motion at the surface from an input earthquake recorded at bedrock, applied at the base of the model, and propagating upward. The choice of the constitutive model to approximate the dynamic behavior of the soils layers during earthquake shaking is a critical issue because such behavior is strongly dependent on the strains developed by the seismic input and by the deposits of the site.

Geotechnical laboratory tests are commonly used to assess the stress-strain relationship of soil under cyclic loading, providing the secant shear modulus G and the hysteretic damping ratio D curves. They describe the variation of shear modulus G and damping ratio D as a function of applied deformations (G/G0 and D curves), also known as hysteretic damping constitutive model. G/G0 and D curves are at the core of the equivalent linear modeling methods (EL) which uniformly associate these parameters with an entire soil layer. The EL procedure consists of the execution of a complete sequence of linear analysis and a subsequent update of the stiffness and damping parameters for the next cycle of linear analysis, until a predefined convergence criterion is satisfied. The EL methods results are considered reliable provided that the strain is below a threshold value, ensuring stable non-linear behavior of the stress-strain relationship. Vucetic (1994) suggest a conventional threshold for the EL method in the strain range of about 0.02% - 0.1% (at 35% degradation of G/G0), depending on the plasticity index of the soil type, indicating that even for smaller strains, when nonlinear behavior occurs, materials are no longer elastic and become slightly elastoplastic. In such cases, incremental nonlinear analysis (NL) is needed to solve the dynamic problem using a step-by-step integration which modifies the values of the mechanical parameters at each element of the model at every step. The soil behavior is modeled using constitutive models that allow plasticization to occur and require additional mechanical parameters to be fully characterized.

In this study, both EL and NL approaches were implemented using LSR2D (Stacec srl, 2017), a EL code based on a time domain finite element method, and FLAC3D (Itasca Consulting Group, Inc., 2019), a NL code based on a time domain finite difference method. LSR2D, has simulation strategy like QUAD4M (Hudson et al., 1992) but they differ

Table 5
List of the selected waveforms and corresponding metadata for the two scenarios MMF1 and MMF2.

Event time	station	Filename	Repi	Mw	PGA [cm/s2]	EC8 class	Target spectrum
30/10/2016 06:40	NRC	IT.NRC..HG.EMSC-20161030_0000029.C.PSA.ASC	4.6	6.5	476.43	B	MMF1-90th (Mean score 0.077)
15/04/2016 16:25	KMM	BO.KMMF17..HNE.USGS-us20005iis.C.PSA.ASC(*)	4.5	7	−599.83	B	MMF1-90th (Mean score 0.077)
30/10/2016 06:40	CLO	IT.CLO..HG.EMSC-20161030_0000029.C.PSA.ASC(*)	7.8	6.5	−418.62	B	MMF1-90th (Mean score 0.077)
30/10/2016 06:40	T1213	IV.T1213..HN.EMSC-20161030_0000029.C.PSA.ASC(*)	12	6.5	779.27	A	MMF1-90th (Mean score 0.077)
23/10/2004 08:55	NIG1	BO.NIG1C..HN.JP-2004-0002.C.PSA.ASC	15.2	6.6	−706.54	B	MMF1-90th (Mean score 0.077)
30/10/2016 06:40	FCC	IT.FCC..HG.EMSC-20161030_0000029.C.PSA.ASC	11	6.5	−931.14	A	MMF1-90th (Mean score 0.077)
26/12/2003 01:56	BAM	I1.BAM..HN.IR-2003-0041.C.PSA.ASC(*)	11.8	6.5	780.92	B	MMF1-90th (Mean score 0.077)
23/10/2004 08:55	NIG13	BO.NIG13.00.HN.JP-2004-0002	5.4	6.6	1285.39	B	MMF2-90th (Mean score 0.142)
23/10/2004 08:55	NIG1D	BO.NIG1D.00.HN.JP-2004-0002	15.4	6.6	656.04	B	MMF2-90th (Mean score 0.142)
15/04/2016 16:25	KMMF	BO.KMMF17.00.HN.USGSus20005iis	4.5	7	−599.834	B	MMF2-90th (Mean score 0.142)
13/06/2008 23:43	IWT33	BO.IWT33.00.HN.EMSC20080613_0000091	2.7	6.9	1133.44	B	MMF2-90th (Mean score 0.142)
23/10/2004 08:55	NIG1D	BO.NIG1D.00.HN.JP-2004-0002	15.4	6.6	820.44	B	MMF2-90th (Mean score 0.142)
13/06/2008 23:43	IWT33	BO.IWT33.00.HN.EMSC20080613_0000091	2.7	6.9	1387.43	B	MMF2-90th (Mean score 0.142)
23/10/2004 08:55	NIG1C	BO.NIG1C.00.HN.JP-2004-0002	15.2	6.6	−706.54	B	MMF2-90th (Mean score 0.142)

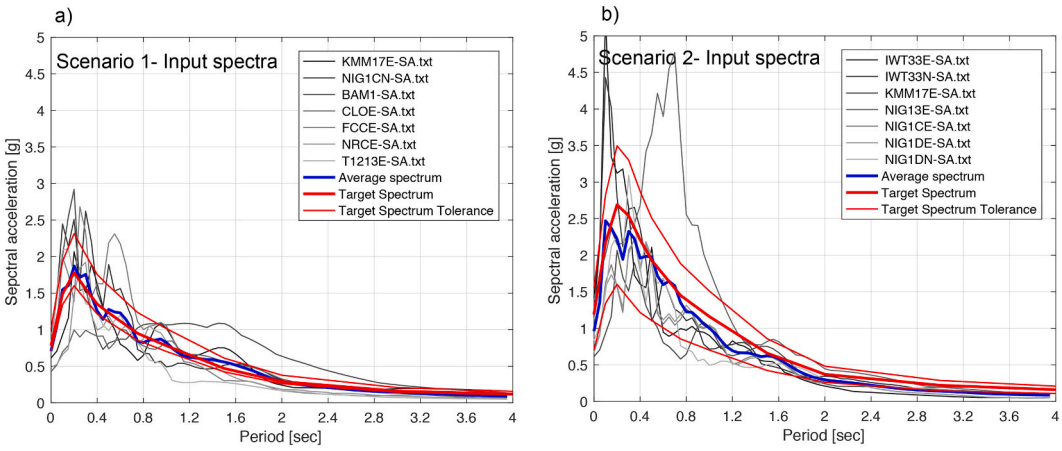

Fig. 11. Spectrum-compatible sets of records for the scenarios a) MMF1 and b) MMF2.

in the way boundary conditions are modeled: LSR2D implemented viscous dampers also at the edges of the domain area using free-field columns in addition to the compliant base.

FLAC3D, is a three-dimensional explicit finite difference program which uses Lagrangian analysis for the solution of various geo-mechanical problems. Its dynamic option allows modeling of wave propagation modeling and provides several mechanical constitutive models which can either be used alone or coupled together. Despite being a 3D code, by using a model set up with an out-of-plane thickness of a few elements it can be used in bidimensional settings. The boundary conditions rely on the use of absorbing "quiet" boundaries, based on the viscous boundaries developed by Lysmer and Kuhlemeyer (1969), as well as on a free-field model which prevents distortion of the incoming waves by the lateral quiet boundary. It consists of four planes on the side boundaries of the model, and four column free-field grids at the corners. The lateral boundaries of the mesh are coupled to the free-field grid by viscous dashpots (Itasca Consulting Group, Inc., 2019). Both codes use as input a vertically incident P-SV wavefield assuming plane-wave conditions.

In applying FLAC3D in this study, we have coupled a hysteretic damping model and the Mohr-Coulomb failure criterion (MC + hyst) and Fig. S3 (Appendix) shows the coupled curve (red curve) along with the hysteretic damping (green curve) and the MC model (blue curve). The decay curve of hysteretic damping is used by FLAC3D to calculate the values of shear stress only in the part of the curve where the model of MC remains stable (horizontal section of the blue curve). When the strain reaches the failure deformation of the MC, the stress values are obtained from the MC curve (red curve). The mechanical parameters needed for Mohr-Coulomb failure criterion are the angle of friction and the cohesion values. For the hysteretic damping model an analytical formulation of Darendeli (2001) curves was adopted, which change with depth to adapt its values to the confinement pressure.

This approach allows us to fully use the characteristics of the software, where the constitutive model is not uniformly associated with a soil layer, as per the EL method, but assumes different values for each model element. In the following, the subsoil model is described and a comparative test of EL and NL simulation is presented with the result of the NL simulations shown in terms of acceleration response spectra.

6.1. Geological model

The investigated site is located at the S-W boundary of the Sulmona basin, which is filled with a sequence of slow velocity continental deposits of lacustrine, fluvial, and alluvial environment with lithologies spanning from silt to sand and gravel, and has a maximum estimated thickness of ~450 m. The CP area lies at the SE edge of the present alluvial plain, in a terraced flat area slightly degrading towards a seasonal river, a tributary of the main Gizio River, and it is backed by the small calcareous relief of the Colle Scipione (Fig. 3 and Fig. 12). Here the bedrock is much shallower, therefore local amplification of the seismic motion is expected to be at a higher frequency. The seismic response of the Sulmona basin has been investigated by many authors (Di Giulio et al., 2016, Rinaldini et al., 2007, Yelikaya and Mercanlig, 2020, Villani et al., 2014) and by microzoning activity (MS1 available at https://protezionecivile.regione.abruzzo.it/index.php/microzonazione).

The geologic formation outcropping in the plain area is the "*Sintema* di *Catignano*", and is formed by middle-Pleistocene gravelly-sand and sandy-silt alluvial deposits, while the small reliefs are made by "*Calcari Ciclotemici a Requiene*", a lower Cretaceous micritic limestone (Note Illustrative Carta Geologica d'Italia CARG, Foglio 369 Sulmona https://www.isprambiente.gov.it/Media/carg/369_SULMONA/Foglio.html).

A subsoil model, constrained by several geologic, geophysical, and geotechnical investigations made for a previous site response analyses following the NTC2018 approach, was provided by MISE DGISSEG (MISE DGISSEG Report, hereinafter referred to as RSL), reconstructed as a result of 3 surveys performed between 2004 and 2018.

The surveys included eight continuous geognostic drillings down to 40 m of depth with samples collected for laboratory tests in each lithological unit at different depths. Three drillings were equipped for Down-hole testing, and several MASW, HVSR, P and S waves seismic tomography were performed. Two perpendicular geological cross-sections had already been drawn: i) a NNW-SSE trending, from the limestone relief to the SSE of the site, towards the Vella River on the NNW, about 250 m long (Fig. 12b); and ii) WSW-ENE trending, running parallel to the basin edge. The latter shows no relevant lateral heterogeneities confirming the roughly lateral extension of the geometry shown in the NNW-SSE cross-section and indicating that a bi-dimensional modeling in the NNW-SSE direction can reproduce the site response of the investigated site. Fig. 12b shows the geological cross-section at the base of the model.

The lithostratigraphy of the area had been summarized into three layers overlying the limestone bedrock with S-wave velocity of 900 m/s. From the top to the bottom, they are: 1) a soil with a maximum thickness of about 2 m and a S-wave velocity of 230 m/s; 2) a gravelly sand and sandy gravel layer with a maximum thickness of 30 m, and a S-wave velocity of 320 m/s; 3) a clay layer with a maximum thickness of 12 m and a S-wave velocity of 300 m/s. Table 6 lists the mechanical parameters used to approximate the soil properties.

6.2. Numerical simulation

The cross-section modeled is 300 m long, 50 m longer than the geological cross-section, and has its S boundary extended to the calcareous relief. Its N boundary is 'open', i.e. the soft deposits are not

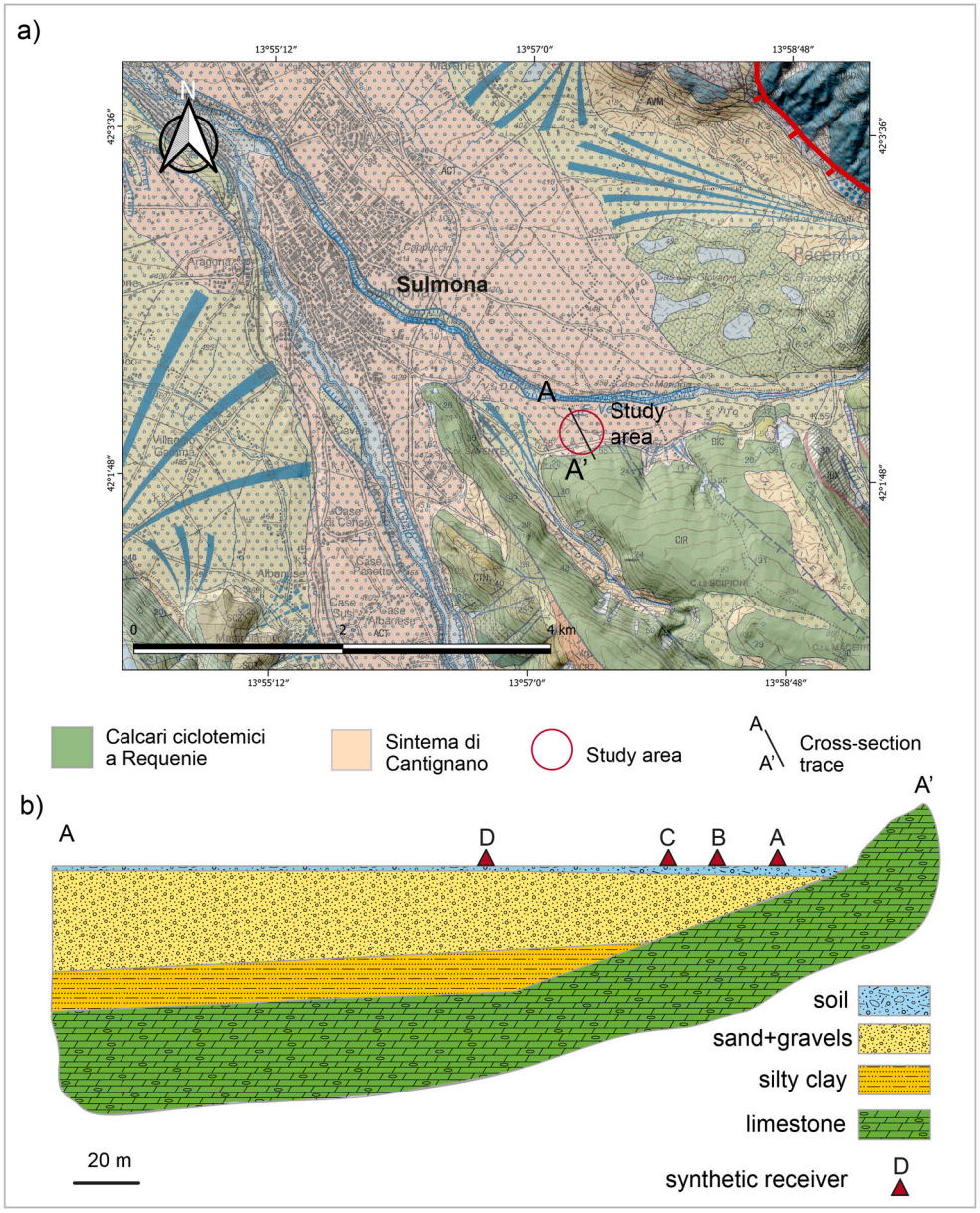

Fig. 12. Detail of Fig. 3 geological map (a) and a sketch of the NNW-SSE geological cross-section with a lithological legend (b).

Table 6
Mechanical parameters for the numerical simulations.

Lithotype	ρ	Vs	n	G (10^{-8})	K(10^{-8})	f	c	Model	(G/G_0)
Soil	1600	230	0.45	0.85	8.18	38	0	MohrCoulomb	Darendeli
Sand - gravel	2200	320	0.35	2.25	6.76	38	0	Mohr-Coulomb	Darendeli
Clay	2000	300	0.40	1.80	8.40	26	10–4	Mohr-Coulomb	Darendeli
Limestone	2500	900	0.25	20.3	0.34	–	–	Elastic	–

Cohesion = c | Poisson Ratio = n | Friction angle = f | Bulk Modulus = K | Shear Modulus = G; Unit of measurement: Vs (m/s); ρ (Kg/m^3); f (KN/m^2); G (Pa).

contained within the stiff calcareous deposits. An open model has two issues. Firstly, it is an unrealistic representation of the investigated site, which is in a valley surrounded by limestone reliefs. In this case, given the strong impedance contrast between the alluvial valley's softest sediment and the limestone reliefs that board them, local waves are generated and trapped within the basin, bouncing back and forth in the soft deposits and giving rise to long-lasting signals. To take these effects into account, a section that crosses the valley and ends to the N on the relief of Mt. Morrone should have been reconstructed. Unfortunately, the data available were not sufficient to constrain such cross-section with any accuracy. Secondly, being an artificial numerical boundary, it gives rise to reflections of the outward propagating waves back into the model, without the needed energy radiation. To cope with the second issue, the "free field" boundary condition has been used in both EQ and NL codes. Fig. 13 shows the grid created in FLAC3D to discretize the model area. It consists of a structured grid with a hexahedral brick shape with size of 2x3x2 meters in the x,y,z-direction. It allows us to recover signals at frequency up to 10 Hz following the $h = Vs/10*f_{max}$ criteria as

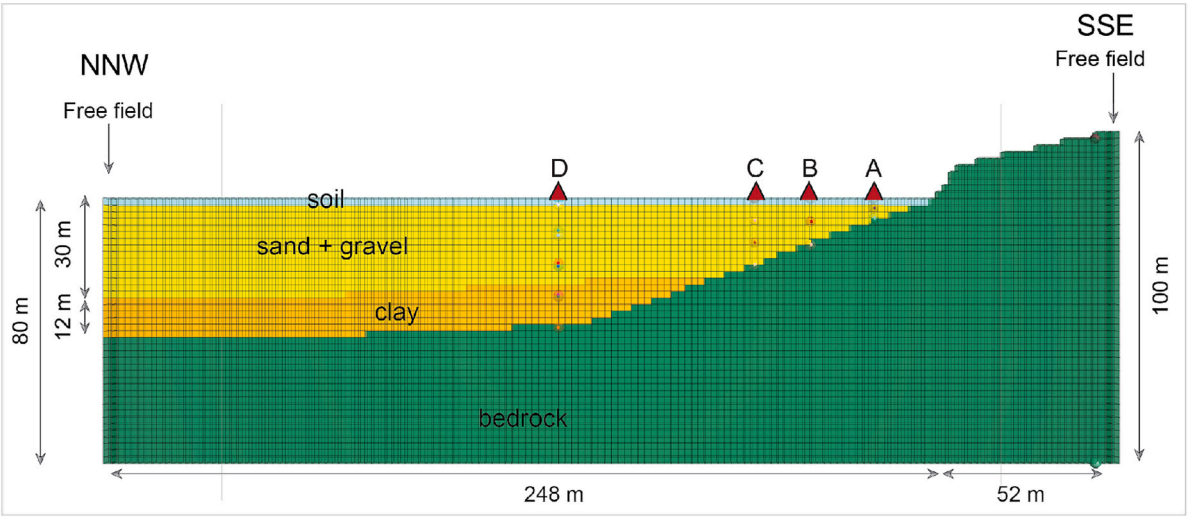

Fig. 13. Subsoil model and structured mesh produced by FLAC3D. Arrows show the position of the free-field planes. Triangles show where synthetics have been calculated at surface.

suggested by Itasca Consulting Group, Inc. (2019), which implies sampling 10 times in the smallest wavelength. For the unstructured mesh used by LSR2D, we have selected a triangle element shape with a variable size depending on the layer velocity following the $h = V_s/160$ implemented criteria by Stacec srl (2017), which allows us to recover signals up to 20 Hz implying sampling 8 times in the smallest wavelength. As an initial approach to modeling, the EL method was tested evaluating the surface ground motion and the strain level induced by one of our selected earthquakes recordings.

In Fig. 14 the response spectra of the 15/04/2016 01:56 Mw 7.0 event of the MMF1 scenario (PGA =0.61), for EL and NL simulation, show a highly damped EL response for $T < 0.6$ s. Using as input the 26/12/2003 01:56 M_w 6.5 (MMF1 scenario, PGA = 0.8) no convergence was reached by the EL code, since the deformation goes well beyond the strain ranges available in the G/G0 curves ($1*10^{-3}$). The strain level reached by NL code is of $\gamma_{clay} = 1*10^{-3}$ and $\gamma_{surface} = 7*10^{-3}$ but, using the coupled constitutive models (MC + H_{yst} see Fig. S3), the NL code can handle such a deformation level without introducing excessive damping. A movie of a FLAC3D run showing acceleration and strain time histories as well as a strain cross-section is available in the Appendix (Fig. S4a) together with some snapshots of the entire movie (Fig. S4b). Following this test, the modeling work was oriented towards the use of FLAC3D. A numerical simulation was run for each of the seven earthquakes associated with the MMF1 and MMF2 scenarios. To capture the lateral heterogeneity of the model, synthetics were calculated at surface receivers located at increasing distances from the basin edge (site A to D, Fig. 12 and Fig. 13). Sites A to C have depth to bedrock <30 m (from about 3 to 23 m) and S-wave velocity which corresponds to Soil Type E, while Site D depth to bedrock is about 36 m and S-wave velocity corresponds to Soil Type C (NCT2018).

6.3. *Results in terms of response spectra*

For each synthetic accelerogram an elastic acceleration response

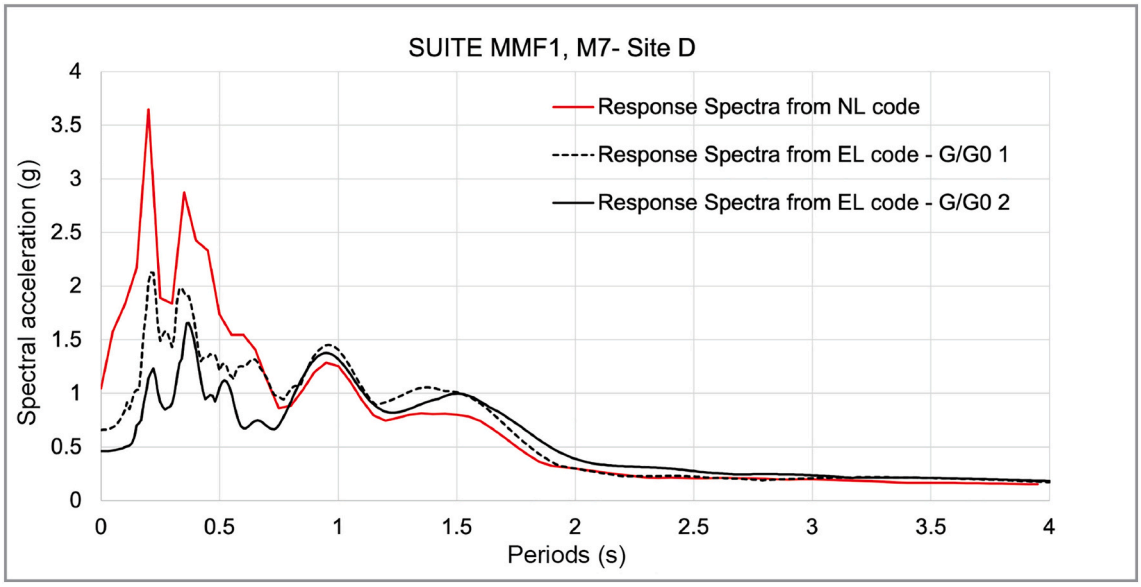

Fig. 14. Acceleration response spectra of the 15/04/2016 01:56 Mw 7 event (PGA 0.61 g) of the MMF1 scenario – for EL and NL simulation, showing a highly damped EL response for $T < 0.75$ s. In the EL modeling, the decay curves are EPRI (Electric Power Research Institute, 1993) and Lanzo et al. (2011) for G/G01, and Darendeli (2001) for G/G02 see Table S1–4.

spectrum with a 5% damping is computed. Individual response spectra are then averaged for each scenario and for each site (A-D). Table 7 lists the peak ground acceleration (PGA) values, which represent the anchor point of the spectra at period $T = 0$. There is a general tendency for PGA to increase moving from sites A to D where the plain deposits are thicker. Site A does not show a relevant amplification effect for MMF1, while for MMF2 a deamplification effect is evident. Such a pattern is linked to the geological and geotechnical characteristics of the sites.

However, PGA value is only one of the parameters describing strong motion that can be obtained from the modeling and might not be particularly relevant. For design purposes the most useful comparison concerns the spectral shape within the most significant period range.

Fig. 15 show average acceleration response spectra for MMF1 and MMF2 Scenario, as well as their individual spectra, to describe the spectral ordinates variability from the average values. To facilitate discussion and drive conclusions, the input target spectra and the NCT2018 spectra are also plotted for reference in the same figure. In particular: i) the normalized design spectra provided by the NTC2018 for the Ultimate Limit State (ULS) using the simplified soil type approach (hereinafter SC); ii) the average spectra for ULS from the site response analysis following NTC2018 (RSL), e.g. that is using a seismic input compatible to the reference seismic hazard model (MPS04) and EL wave propagation modeling method. Fig. 15b presents only the average acceleration response spectra derived from input events (real) and output events (synthetics).

The results can be summarized as:

- Both scenarios generate shaking levels significantly larger than the building code ones, both for the SC (blue and light blue curves in Fig. 15) and for the RSL approach (magenta and light green curves in Fig. 15). More specifically, the MMF2 scenario-based spectra exceed SC and RSL up to $T = 2$ s while the MMF1 scenario-based spectra exceed SC and RSL up to $T = 0.8$ s. Their maximum value of $S_a(T)$ is roughly a factor of 2 of the RSL one and a factor of 3 of the SC one.
- The maximum $S_a(T)$ reach extreme values at site D in both scenarios. For MMF2, the $S_a(T)$ peaks equal to 3.5 g while in a $T = 0.1$–0.5 s range values are around 3 g. For MMF1, the maximum $S_a(T)$ is 3.3 g while in the range T = 0.1–0.5 s $S_a(T)$ maximum values are around 2.1. There are some notable exceptions, with one simulation for both scenarios reaching the highest $S_a(T)$ value at 0.7 s. These high values are in the input data possibly due to a source effect. Note that the input motion from MMF1 has a $S_a(T)$ level similar to the output motion of RSL.
- At sites A to C the predicted $S_a(T)$ values are significant but consistently lower than those predicted at site D.
- At sites A and B amplification is restricted into a very narrow range of T = 0.1–0.2 s, while for larger periods the input and output spectra are similar. Site A exhibits deamplification between 0.2 and 0.5 s in both scenarios. It can be inferred that nonlinear behavior of the soil is responsible for these patterns. For the sharp peak at short periods we observe a lower amplification for Scenario 2, potentially related to nonlinear soil behavior, as suggested by the strain pattern described by Fig. S4abc (Appendix A).
- A movie (Fig. S4a) and some snapshots (Fig. S4b), available as supplementary material (Appendix A), show the strain pattern as well as acceleration and strain time series obtained using as bedrock input an earthquake recording of the MMF1 Scenario. Site A is within an area of maximum strain, where elasto-plasticity and damping occur, while site D is on top of a sigmoidal-shaped area of deposits with the minimum level of strain, possibly still in a predominant elastic domain. Therefore, the different strain levels can explain their different behavior and the transition from amplifying to de-amplifying behavior. Moreover, the clay layer appears to absorb much of the strain acting as natural seismic isolator.
- Fig. 15b shows that the output maximum $S_a(T)$ increases by roughly 29% for MMF2 and 46% for MMF1.
- Fig. 16 shows a shift of the amplified band towards shorter periods in both scenarios, moving from site D, characterized by a thickness of the soft sediment of about 40 m, to site A, where the thickness is about 3 m (Fig. 13). Also, the amplitude of $S_a(T)$ decreases with the same pattern, probably because of the above-mentioned distribution of strain within the deposits (Fig. S4).
- Fig. 16 shows that the differences between the various results tend to decrease for periods of oscillation greater than $T = 1.2$–1.6 s where the amplification effects are significantly reduced.

Table 7
PGA values (g) at surface control point from average 5% damping elastic response spectra.

Scenario	M	Input	D	C	B	A
MMF1	6.7	0. 71	1.1	0.89	0.91	0.74
MMF2	7.0	0. 96	1.3	1.2	1.20	0.89

7. Findings and discussion

In this study a novel and comprehensive approach to assess site-specific ground response to earthquakes in a near-fault setting has been presented with reference to the Case Pente (CP) site located at the edge of the Sulmona basin. At CP, an industrial facility was planned to be built and MISE DGISSEG asked to the authors, an interdisciplinary team comprised of geologists, geophysics, engineers, to revise the seismic response and its seismic input for design purposes according to a performance-based design approach, taking into account a most prudential shaking scenario.

This proposed GRA methodology has been developed starting from the concern that in the near-fault condition the seismic input at the bedrock provided by the reference seismic hazard model on rock might be biased, not necessarily a conservative estimation of the seismic demand, as observed in recent Italian earthquakes, namely the 2009 L'Aquila, the 2012 Emilia, and 2016–2017 Central Italy seismic sequences. Under these circumstances, it is of engineering relevance to assess such larger seismic shaking actions to the built environment and take them into account, preferably within a performance-based assessment and design approach, with the final aim to reduce and minimize the socio-economic impact and enhance the community resilience (Pampanin, 2012).

To pursue this goal, a multidisciplinary methodology (Fig. 1) subdivided into 4 steps has been applied: 1) geometric and kinematic parametrization of the major faults near the site, 2) definition of a target response spectra based on a deterministic scenario analysis (SSHA), validated against a time-dependent and time-independent probabilistic approach (PSHA); 3) retrieval of accelerograms from earthquakes databases spectrum-compatible to the target response hazard spectrum; 4) non-linear numerical modeling of the soil response. Each step has brought its conclusions, some of which are novel, which are used as input for the next methodological step:

STEP 1 - This involves a critical review of the published seismotectonic literature concerning the Mt. Morrone and Maiella-Porrara faults, aimed at exploring the potential of the Mt. Morrone fault to activate alone (Scenario 1 or MMF1) or to activate together with the Maiella-Porrara fault (Scenario 2 or MMF2) as segments of the same seismogenic fault system and to derive their parameters (Table 1-2). In Scenario 2, rupture nucleates on one of these two structures and propagates along the nearby fault segment/s. Such an extended fault system, highly plausible in terms of the structural and kinematic relationship between the active tectonic structures, has never been the object of a seismic hazard study before.

STEP 2 - Based on MMF1 and MMF2 parameters, a SSHA estimation of seismic hazard was carried out using a scenario-based approach by assessing for each fault and each magnitude a distribution of spectral ordinates predicted by the set of selected GMMs as well as a time-

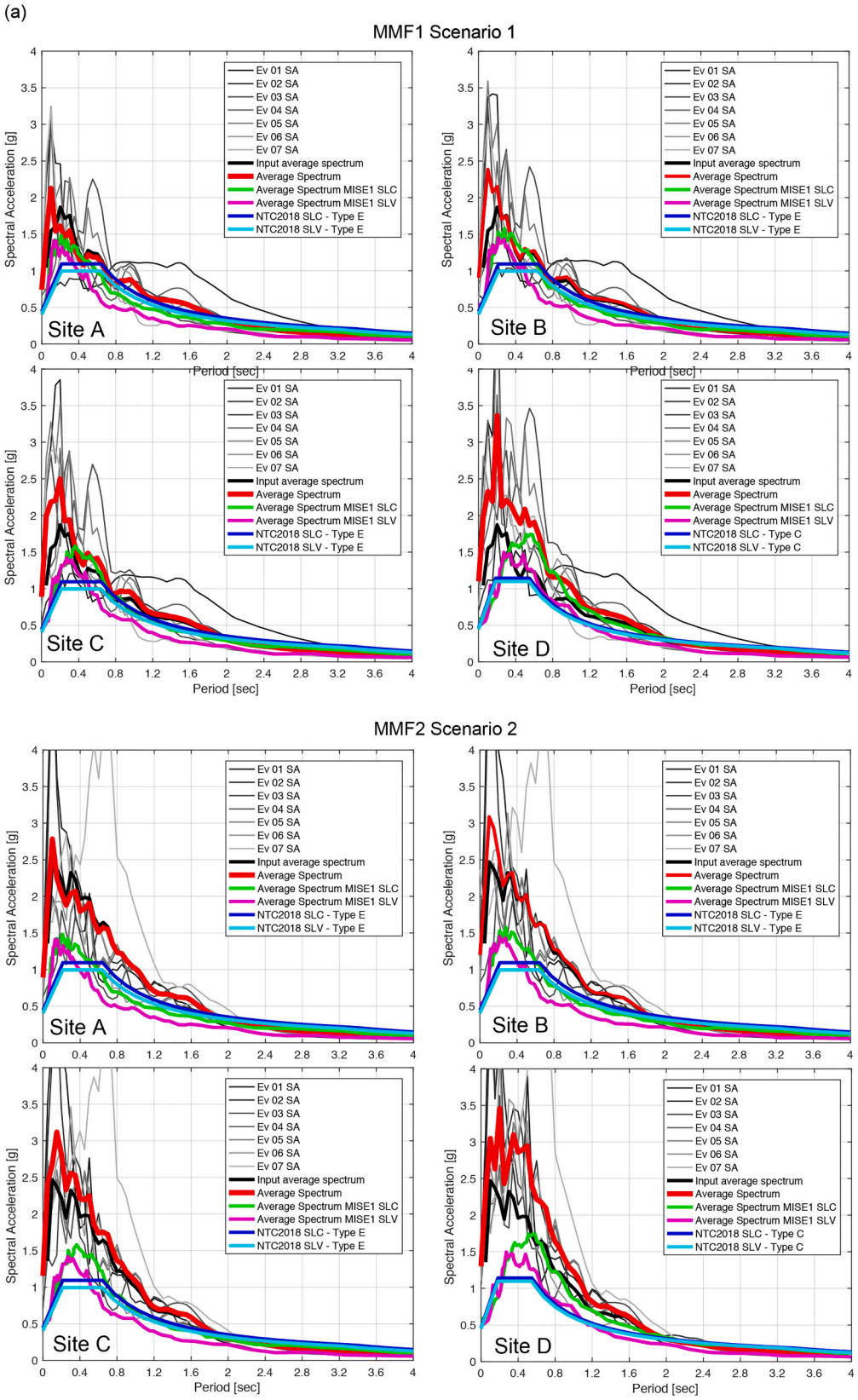

Fig. 15. a. Comparison among average acceleration response spectra from synthetics for MMF1 (1) and MMF2 (2) Scenarios for sites A-D. Output surface spectrum (red line), input bedrock spectrum (black line), RSL spectrum for limit state design ULS (green line near collapse, magenta line life safety) and SC spectrum for soil type C and E. All the individual response spectra from simulation synthetics are drawn with gray lines Fig. 15b. Comparison between average acceleration response spectra derived from input events (real) and output events (synthetic) for Scenario 1 - MMF1 and Scenario 2 - MMF2 at site A-D. (For interpretation of the references to colour in this figure legend, the reader is referred to the web version of this article.)

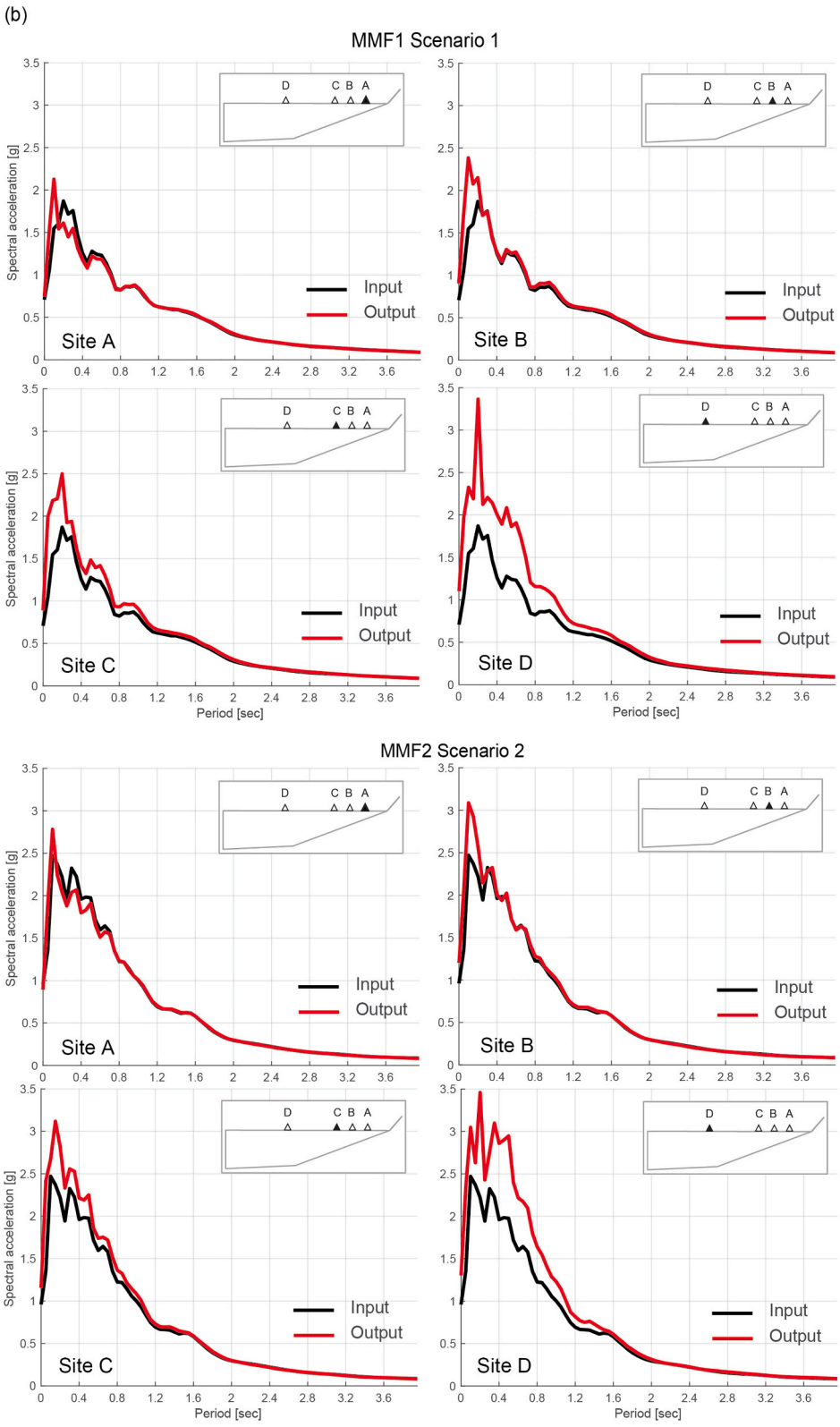

Fig. 15. (*continued*).

dependent and a time-independent PSHA using MMF2 both at a rock site.

The outcomes of the SSHA approach from both scenarios are compared with the results of the PSHA realized, considering Scenario 2 (MMF2), its slip rate uncertainty and two different occurrence models to validate the choice of target spectra. The comparison between the two approaches (Fig. 9) taking into account only the MMF2 computations, shows how the 90th percentile for Scenario 2 (MMF2) is comparable to the PSHA renewal model. In particular, PSHA renewal model results are strongly influenced by the MMF2 structure being in a condition of seismic gap, with its elapsed time comparable to its recurrence time. In addition Fig. 9 shows that the MMF2 scenario spectra is much higher

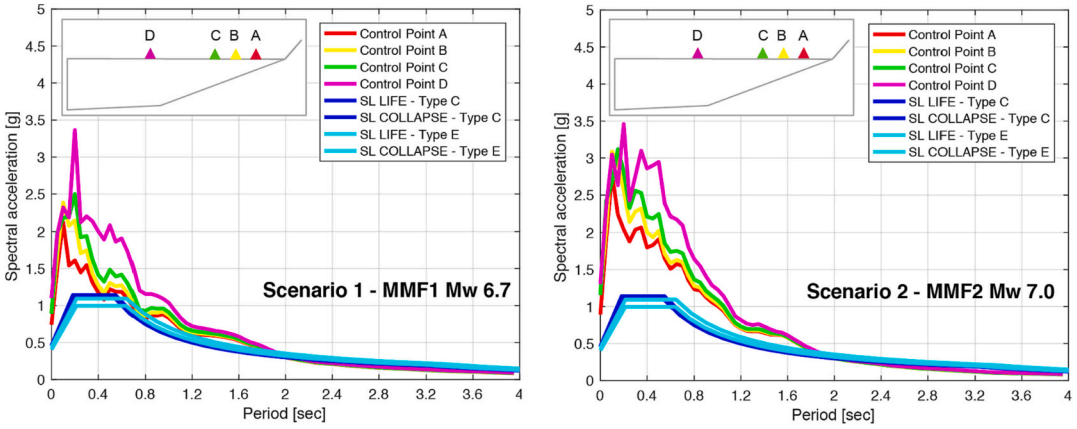

Fig. 16. Comparison between response spectra for MMF1 and MMF2 at sites A-D. Note the decrease of spectral amplitude from D to A and of the spectral amplification band. As a term of reference: NTC 2018 spectra for limit state design Life and Near Collapse for soil type C (blue) and soil type E (light blue) corresponding respectively to sites D and A-C are included. (For interpretation of the references to colour in this figure legend, the reader is referred to the web version of this article.)

than the PSHA time-independent spectra, which is an average of all the sources included in this computation. Starting from these observations we decided to use the 90th percentile of SSHA analyses to select the input accelerograms to be used for the ground shaking numerical simulation at CP. Furthermore, the 90th percentile is of particular importance in the structural field, as it is commonly accepted as an upper limit for performance-based earthquake engineering acceptance criteria. This limit supports the designers in identifying critical ground motions for structural damage studies with a certain level of confidence (Dhakal et al., 2006; Cornell et al., 2002; FEMA, 2000).

Actually, from the initial work developed in 2018–19, the selection has moved from a curve representing the 95th percentile of the values to the 90th percentile ones. Meanwhile a new GMM model has been released (Lanzano et al., 2019), including the 2012 Emilia-Northern Italy and 2016–2017 Central Italy earthquakes strong motion recordings. With respect to previous GMMs, it produced changes in median and standard deviation predictions - leading to higher predictions for strong near source normal faulting events, at distances below 10 km. This result, that is higher hazard predictions from newer GMMs, has been observed many times and explained by larger values of uncertainty being present in the newer GMMs due to more data availability and their larger standard deviation (Bommer and Abrahamson, 2006). It should also be noted that beyond the threshold of one standard deviation (1 sigma) of the mean scenario, based on the time series currently available in the accelerogram databases, the retrieved ground motion records following the spectro-compatibility rules would be the same for the 90th and the 95th percentile, and agrees well with the PGA values derived from a probabilistic time-dependent approach.

STEP 3 - The scenario-based spectra associated with 90% of the distribution were then used to select the spectrum-compatible accelerograms, (Bommer and Acevedo, 2004). Due to the high magnitude associated with MMF1 and MMF2 scenarios it was not possible to select the input accelerograms from the italian events database, and to respect the requirement of normal fault source mechanism. The selected waveforms refers to earthquakes that occurred worldwide and also include accelerograms affected by near-source effects, such as large velocity pulse.

STEP 4 - Numerical modeling focused on a representative two-dimensional section of the survey site following a comparative test between the strain and acceleration level developed by equivalent-linear (EL) and nonlinear (NL) numerical codes for a M_w7 earthquake (Fig. 14). Because a relevant damping appears for deformation levels reaching values for which the EL method is commonly considered no longer reliable (Vucetic, 1994), the analyses were developed using the NL approach by FLAC3D based on the Mohr-Coulomb constitutive model (MC) coupled to a hysteretic damping model (HYST).

The acceleration response spectra (Fig. 15b-16) show a very clear shift of the amplified band towards shorter periods in both scenarios, moving from site D to site A. The maximum S_a(T)reach extreme values at site D in both scenarios. The S_a(T) peak is equal to 3.3 g for MMF1 and 3.5 g for MMF1, while in a band that extends from $T = 0.1$ to $T = 0.5$ s values are around 2.1 g and 3 g, respectively for MMF1 and MMF2. Taking into account the NTC2018 acceleration spectra, the MMF1 values are significantly higher for periods up to $T = 0.8$ s, while in the MMF2 case, the output spectra significantly exceed the NCT2018 up to $T = 2$ s periods. The GRA maximum value of S_a(T) is roughly a factor of 2 of the RSL one and a factor of 3 of the SC one. Fig. 15b shows that the output maximum S_a(T) increases by roughly 29% for MMF2 and 46% for MMF1 scenario. The non-linear behavior of the soils has strongly influenced the results by producing reduced amplification effects and, in some cases, de-amplification phenomena. However, the seismic motion values are higher than those provided by the NTC2018, using both the simplified approach for soil categories (SC) and the one based on the local seismic response analyses (RSL) starting from the basic seismic hazard. Fig. 16 clearly shows that the differences between the various results tend to decrease for periods of oscillation T >1.2–1.6 s where the amplification factors are significantly reduced. The largest amplification factors are found for periods T <0.8 s. These findings suggest addressing design strategies towards using natural periods of vibration where small spectral accelerations are predicted.

8. Conclusion

The key outcome of this complex study is the confirmation of the need, on one hand, as well as the real opportunity, on the other, to implement multiple scenario approaches for site-specific seismic response studies in near-fault areas, coupled and integrated with nonlinear numerical simulations.

Their combined use can better capture the shaking effect in near-field conditions, avoiding possibly unconservative estimations of the seismic actions and in view of a more robust performance-based approach for either new design and/or assessment/retrofit purposes of the built environment.

Using the scenario-based spectrum-compatible accelerograms, the fully nonlinear GRA obtains a maximum value of S_a(T) roughly larger by a factor of 2 when compared to the RSL one and by a factor of 3 when compared to the SC one.

CRediT authorship contribution statement

Paola Bordoni: Conceptualization, Methodology, Formal analysis, Visualization, Writing – original draft, Writing – review & editing, Project administration. **Stefano Gori:** Conceptualization, Writing – original draft, Writing – review & editing, Investigation. **Aybige Akinci:** Conceptualization, Methodology, Visualization, Writing – original draft, Writing – review & editing. **Francesco Visini:** Methodology, Formal analysis. **Sara Sgobba:** Data curation, Software, Writing – original draft, Writing – review & editing. **Francesca Pacor:** Writing - original draft, Writing - review & editing. **Fabrizio Cara:** Software, Visualization. **Stefano Pampanin:** Writing - review & editing. **Giuliano Milana:** Conceptualization, Methodology, Project administration, Writing - original draft, Writing - review & editing. **Carlo Doglioni:** Conceptualization, Funding acquisition.

Declaration of Competing Interest

The authors declare that they have no known competing financial interests or personal relationships that could have appeared to influence the work reported in this paper.

Data availability

Data will be made available on request.

Acknowledgments

This research work was developed between 2018 and 2019, addressing a request of the Italian Ministry of the Economic Development (formerly MISE, now Ministry of environment and energetic safety, MASE) through the General division for the infrastructures and the safety of energy and geomining systems (DGISSEG).

Dr. Carlo Meletti is acknowledged for helping to set up the study and sharing in fruitful discussions. The support and assistance of dr. Augusto Lucarelli from Itasca Consulting as well as Harpaceas srl in the use of the FLAC3D code is acknowledged.

Dr. Peter Jewison Hill is acknowledged for improving the readability of the paper.

Appendix A. Supplementary data

Supplementary data to this article can be found online at https://doi.org/10.1016/j.enggeo.2022.106970.

References

Akinci, A., Galadini, F., Pantosti, D., Petersen, D., Malagnini, L., Perkins, D., 2009. Effect of time dependence on probabilistic seismic hazard maps and deaggregation for the central Apennines, Italy. Bull. Seismol. Soc. Am. 99, 585–610.

Akinci, A., Perkins, D., Lombardi, A.M., Basili, R., 2010. Uncertainties in the estimation of the probability of occurrence of strong earthquakes from individual seismological sources in the Apennines. Italy, J. Seismol. 14, 95–117.

Akinci, A., Vannoli, P., Falcone, G., Taroni, M., Tiberti, M.M., Murru, M., Burrato, P., Mariucci, M.T., 2017. When time and faults matter: towards a time-dependent probabilistic SHA in Calabria, Italy. Bull. Earthq. Eng. 15, 2497–2524.

Akinci, A., Moschetti, M.P., Taroni, M., 2018. Ensemble smoothed seismicity models for the new Italian probabilistic seismic hazard map. Seismol. Res. Lett. 89, 1225. https://doi.org/10.1785/022018015.

Al Shawa, O., Atzori, S., Doglioni, C., Liberatore, D., Sorrentino, L., Tertulliani, A., 2021. Coseismic vertical ground deformation vs. intensity measures: examples from the Apennines. Eng. Geol. 293, 106323 https://doi.org/10.1016/j.enggeo.2021.106323.

Anderson, J.G., Luco, J.E., 1983. Consequences of slip rate constraints on earthquake occurrence relations. Bull. Seismol. Soc. Am. 73, 471–496.

Bard, P.-Y., Bouchon, M., 1980a. The seismic response of sediment-filled valleys. Part 1. The case of incident SH waves. Bull. Seismol. Soc. Am. 70, 1263–1286. https://doi.org/10.1785/BSSA0700041263.

Bard, P.-Y., Bouchon, M., 1980b. The seismic response of sediment-filled valleys. Part 2. The case of incident P and SV waves. Bull. Seismol. Soc. Am. 70, 1921–1941. https://doi.org/10.1785/BSSA0700051921.

Bard, P.-Y., Bouchon, M., 1985. The two-dimensional resonance of sediment-filled valleys. Bull. Seismol. Soc. Am. 75, 519–541. https://doi.org/10.1785/BSSA0750020519.

Bindi, D., Pacor, F., Luzi, L., et al., 2011. Ground motion prediction equations derived from the Italian strong-motion database. Bull. Earthq. Eng. 9, 1899–1920.

Bindi, D., Massa, M., Luzi, L., Ameri, G., Pacor, F., Puglia, R., Augliera, P., 2014. Pan-European ground-motion prediction equations for the average horizontal component of PGA, PGV, and 5%- damped PSA at spectral periods up to 3.0 s using the RESORCE dataset. Bull. Earthq. Eng. 12 (1), 391–430.

Bommer, J.J., Abrahamson, N.A., 2006. Why do modern probabilistic seismic- hazard analyses often lead to increased hazard estimates? Bull. Seismol. Soc. Am. 96, 1967–1977. https://doi.org/10.1785/0120060043.

Bommer, J.J., Acevedo, A.B., 2004. The use of real earthquake accelerograms as input to dynamic analysis. J. Earthq. Eng. 8 (4), 1–50.

Boncio, P., Lavecchia, G., Pace, B., 2004. Defining a model of 3D seismogenic sources for Seismic Hazard Assessment applications: the case of central Apennines (Italy). J. Seismol. 8, 407–425.

Bordoni, P., Di Giulio, G., Haines, A.J., Cara, F., Milana, G., Rovelli, A., 2010. Issues in choosing the references to use for spectral ratios from observations and modeling at Cavola Landslide in Northern Italy. Bull. Seismol. Soc. Am. 100, 1578–1613. https://doi.org/10.1785/0120090116.

Bosi, C., Galadini, F., Giaccio, B., Messina, P., Sposato, A., 2003. Plio-Quaternary continental deposits in the Latium-Abruzzi Apennines: the correlation of geological events across different intermontane basins, I1. Quaternario 16, 55–76.

Carminati, E., Doglioni, C., 2012. Alps vs. apennines: the paradigm of a tectonically asymmetric Earth. Earth-Sci. Rev. 112, 67–96.

Cauzzi, C., Faccioli, E., Vanini, M., Bianchini, A., 2015. Updated predictive equations for broadband (0.01–10 s) horizontal response spectra and peak ground motions, based on a global dataset of digital acceleration records. Bull. Earthq. Eng. https://doi.org/10.1007/s10518-014-9685-y.

Ceccaroni, E., Ameri, G., Gomez Capera, A.A., Galadini, F., 2009. The 2nd century AD earthquake in Central Italy: archaeoseismological data and seismotectonic implications. Nat. Hazards 50, 335–359.

Cheloni, D., Giuliani, R., D'Anastasio, E., Atzori, S., Walters, R.J., Bonci, L., D'Agostino, N., Mattone, M., Calcaterra, S., Gambino, P., et al., 2014. Coseismic and post-seismic slip of the 2009 L'Aquila (Central Italy) MW 6.3 earthquake and implications for seismic potential along the Campotosto fault from joint inversion of high-precision levelling, InSAR and GPS data. Tectonophysics 622, 168–185.

Cheloni, D., Falcucci, E., Gori, S., 2019. Half-graben rupture geometry of the 30 October 2016 M W 6.6 Mt. Vettore-Mt. Bove Earthquake, Central Italy. J. Geophys. Res. Solid Earth. https://doi.org/10.1029/2018JB015851.

Chiaraluce, L., Di Stefano, R., Tinti, E., Scognamiglio, L., Michele, M., Casarotti, E., Cattaneo, M., De Gori, P., Chiarabba, C., Monachesi, G., Lombardi, A., Valoroso, L., Latorre, D., Marzorati, S., 2017. The 2016 Central Italy seismic sequence: a first look at the mainshocks, aftershocks, and source models. Seismol. Res. Lett. 88, 757–771.

Chioccarelli, E., Iervolino, I., 2010. Near-source seismic demand and pulse-like records: a discussion for L'Aquila earthquake. Earthq. Eng. Struct. Dyn. 39, 1039–1062. https://doi.org/10.1002/eqe.987.

Cito, P., Iervolino, I., 2020. Rarity, proximity, and design actions: mapping strong earthquakes in Italy. Ann. Geophys. 63 (6), SE671. https://doi.org/10.4401/ag-8516.

Civico, R., Pucci, S., Villani, F., Pizzimenti, L., De Martini, P.M., Nappi, R., the Open EMERGEO Working Group, 2018. Surface ruptures following the 30 October 2016 Mw 6.5 Norcia earthquake, Central Italy. J. Maps 14 (2), 151–160.

Cornell, C.A., 1971. Probabilistic analysis of damage to structures under seismic loads. In: Dynamic Waves in Civil Engineering. John Wiley & Sons, New York, pp. 473–488.

Cornell, C.A., Jalayer, F., Hamburger, R.O., Foutch, D.A., 2002. Probabilistic basis for 2000 SAC Federal Emergency Management Agency steel moment frame guidelines. ASCE J. Struct. Eng. 128 (4), 526533.

Cosentino, D., Cipollari, P., Marsili, P., Scrocca, D., 2010. Geology of the central Apennines: a regional review. J. Virtual Explor. volume 36. Electronic Edition, ISSN 1441–8142. paper 11In: (Eds.) Marco Beltrando, Angelo Peccerillo, Massimo Mattei, Sandro Conticelli, and Carlo Doglioni, The Geology of Italy, 2010.

D'Amico, M., Felicetta, C., Russo, E., Sgobba, S., Lanzano, G., Pacor, F., Luzi, L., 2020. Italian Accelerometric Archive v 3.1 - Istituto Nazionale di Geofisica e Vulcanologia, Dipartimento della Protezione Civile Nazionale. https://doi.org/10.13127/itaca.3.1.

Darendeli, M.B., 2001. Development of a New Family of Normalized Modulus Reduction and Material Damping Curves (Phd Dissertation). The University of Texas at Austin. http://hdl.handle.net/2152/10396.

Dhakal, R.P., Mander, J.B., Mashiko, N., 2006. Identification of critical ground motions for seismic performance assessment of structures. Earthq. Eng. Struct. Dyn. 35, 989–1008. https://doi.org/10.1002/eqe.568.

Di Domenica, A., Pizzi, A., 2017. Defining a mid-Holocene earthquake through speleoseismological and independent data: implications for the outer Central Apennines (Italy) seismotectonic framework. Solid Earth 8 (1), 161–176.

Di Giulio, G., de Nardis, R., Boncio, P., Milana, G., Rosatelli, G., Stoppa, F., Lavecchia, G., 2016. Seismic response of a deep continental basin including velocity inversion: the Sulmona intramontane basin (Central Apennines, Italy). Geophys. J. Int. 204, 418–439. https://doi.org/10.1093/gji/ggv444.

DISS Working Group, 2021. Database of Individual Seismogenic Sources (DISS), Version 3.3.0: A compilation of potential sources for earthquakes larger than M 5.5 in Italy and surrounding areas. Istituto Nazionale di Geofisica e Vulcanologia (INGV). https://doi.org/10.13127/diss3.3.0 last accessed 07 September 2022.

Doglioni, C., Barba, S., Carminati, E., Riguzzi, F., 2011. Role of the brittle-ductile transition on fault activation. Phys. Earth Planet. Inter. 184, 160–171.

Doglioni, C., Carminati, E., Petricca, P., Riguzzi, F., 2015. Normal fault earthquakes or graviquakes. Sci. Rep. 5, 12110. https://doi.org/10.1038/srep12110.
Electric Power Research Institute, 1993. Guidelines for Determining Design Basis Ground Motions (No. EPRI TR-102293). Electric Power Research Institute, Palo Alto, California. https://www.epri.com/research/products/TR-102293-V5. last accessed 7 September 2022.
Ellsworth, W.L., 1995. Characteristic earthquakes and longterm earthquake forecasts: Implications of Central California seismicity. In: Cheng, F.Y., Sheu, M.S. (Eds.), Urban Disaster Mitigation: The Role of Science and Technology. Elsevier, Amsterdam, pp. 1–14.
Ellsworth, William L., Matthews, M.V., Nadeau, R.M., Nishenko, S.P., Reasenberg, P.A., Simpson, R.W., 1999. A Physically-Based Earthquake Recurrence Model for Estimation of Long-Term Earthquake Probabilities: U. S. Geological Survey Open-File Report 99-522, 23 pp. https://pubs.usgs.gov/of/1999/0522/.
Emergeo Working Group, 2010. Evidence for surface rupture associated with the Mw 6.3 L'Aquila earthquake sequence of April 2009 Central Italy. Terra Nova 22, 43–51.
Faccioli, E., 2006. Seismic hazard assessment for derivation of earthquake scenarios in Risk-UE. Bull. Earthq. Eng. 4, 341–364. https://doi.org/10.1007/s10518-006-9021-2.
Falcucci, E., Gori, S., Moro, M., Fubelli, G., Saroli, M., Chiarabba, C., Galadini, F., 2015. Deep reaching versus vertically restricted Quaternary normal faults: implications on seismic potential assessment in tectonically active regions. Lessons from the middle Aterno valley fault system, central Italy. Tectonophysics 651-652, 186–198. https://doi.org/10.1016/j.tecto.2015.03.021.
Falcucci, E., Gori, S., Peronace, E., Fubelli, G., Moro, M., Saroli, M., Giaccio, B., Messina, P., Naso, G., Scardia, G., Sposato, A., Voltaggio, M., Galli, P., Galadini, F., 2009. The Paganica fault and surface coseismic ruptures caused by the 6 April 2009, earthquake (L'Aquila, central Italy). Seismol. Res. Lett. 80, 940–950.
Falcucci, E., Gori, S., Bignami, C., Pietrantonio, G., Melini, D., Moro, M., Saroli, M., Galadini, F., 2018. The Campotosto seismic gap in between the 2009 and 2016-2017 seismic sequences of Central Italy and the role of inherited lithospheric faults in regional seismotectonic settings. Tectonics 37. https://doi.org/10.1029/2017TC004844.
Faure Walker, J., Boncio, P., Pace, B., et al., 2021. Fault2SHA Central Apennines database and structuring active fault data for seismic hazard assessment. Sci.Data 8 (87), 2021. https://doi.org/10.1038/s41597-021-00868-0.
FEMA, 2000. Recommended seismic evaluation and upgrade criteria for existing welded steel moment frame buildings. In: Report No. FEMA-351, SAC Joint Venture. Federal Emergency Management Agency, Washington DC. https://www.nehrp.gov/pdf/fema351.pdf (last accessed 7 September 2022).
Field, E.H., Jackson, D.D., Dolan, J.F., 1999. A mutually consistent seismic hazard source model for Southern California. Bull. Seismol. Soc. Am. 89 (3), 559–578.
Field, E.H., Biasi, G.P., Bird, P., Dawson, T.E., Felzer, K.R., Jackson, D.D., Johnson, K.M., Jordan, T.H., Madden, C., Michael, A.J., Milner, K.R., Page, M.T., Parsons, T., Powers, P.M., Shaw, B.E., Thatcher, W.R., Weldon II, R.J., Zeng, Y., 2015. Long-term time-dependent probabilities for the third uniform California earthquake rupture forecast (UCERF3). Bull. Seismol. Soc. Am. 105 (2A), 511–543. https://doi.org/10.1785/0120140093.
Galadini, F., Galli, P., 1999. The Holocene paleoearthquakes on the 1915 Avezzano earthquake faults (Central Italy): Implications for active tectonics in central Apennines. Tectonophysics 308, 143–170.
Galadini, F., Galli, P., 2000. Active tectonics in the central Apennines (Italy) - Input data for seismic hazard assessment. Nat. Hazards 22, 225–270.
Galadini, F., Galli, P., 2001. Archaeoseismology in Italy: case studies and implications on long-term seismicity. J. Earthq. Eng. 5, 35–68.
Galli, P., Pallone, F., 2019. Reviewing the intensity distribution of the 1933 earthquake (Maiella, Central Italy). Clues on the seismogenic fault. Alpine and Mediterranean Quaternary 32 2, 1–8.
Galli, P., Galadini, F., Pantosti, D., 2008. Twenty years of paleoseismology in Italy. Earth-Sci. Rev. 88, 89–117.
Galli, P., Giaccio, B., Peronace, E., Messina, P., 2015. Holocene paleoearthquakes and Early-Late Pleistocene slip rate on the Sulmona Fault (Central Apennines, Italy). Bull. Seismol. Soc. Am. 105, 1–13. https://doi.org/10.1785/0120140029.
Gardner, J.K., Knopoff, L., 1974. Is the sequence of earthquakes in Southern California, with aftershocks removed, Poissonian? Bull. Seismol. Soc. Am. 64 (15), 1363–1367.
Gasperini, P., Lolli, B., Vannucci, G., 2013. Empirical calibration of local magnitude data sets versus moment magnitude. Bull. Seismol. Soc. Am. 103, 2227–2246.
Gerstenberger, M.C., Marzocchi, W., Allen, T., Pagani, M., Adams, J., Danciu, L., Field, E., Fujiwara, H., Luco, N., Ma, K.-F., Meletti, C., Petersen, M., 2020. Probabilistic seismic hazard analysis at regional and national scale: state of the art and future challenges. Rev. Geophys. 58 e2019RG000653.
Giaccio, B., Messina, P., Sposato, A., Voltaggio, M., Zanchetta, G., Galadini, F., Gori, S., Santacroce, R., 2009. Tephra layers from Holocene lake sediments of the Sulmona Basin, Central Italy: implications for volcanic activity in Peninsular Italy and tephrostratigraphy in the Central Mediterranean area. Quat. Sci. Rev. 28, 2710–2733.
Giaccio, B., Castorina, F., Nomade, S., Scardia, G., Voltaggio, M., Sagnotti, L., 2012. Revised chronology of the Sulmona lacustrine succession, Central Italy. J. Quat. Sci. 28 (6), 545–551.
Gori, S., 2010. Definition of Seismogenic Sources in Poorly Known Tectonically Active Regions of the Italian Peninsula. Ph.D. Thesis.. Università degli Studi Roma Tre, Roma, Italia.
Gori, S., Dramis, F., Galadini, F., Messina, P., 2007. The use of geomorphological markers in the footwall of active faults for kinematic evaluation: examples from the central Apennines. Boll. Soc. Geol. It. 126, 365–374.
Gori, S., Giaccio, B., Galadini, F., Falcucci, E., Messina, P., Sposato, A., Dramis, F., 2011. Active normal faulting along the Mt. Morrone south-western slopes (central Apennines, Italy). Int. J.Earth Sci. 100, 157–171.
Gori, S., Falcucci, E., Dramis, F., Galadini, F., Galli, P., Giaccio, B., Messina, P., Pizzi, A., Sposato, A., Cosentino, D., 2014. Deep-seated gravitational slope deformation, large-scale rock failure,and active normal faulting along Mt. Morrone (Sulmona basin, Central Italy): Geomorphological and paleoseismological analyses. Geomorphology 208, 88–101.
Haines, A.J., Hulme, T., Yu, J., 2004. General elastic wave scattering problems using an impedance operator approach – I. Mathematical development. Geophys. J. Int. 159, 643–657. https://doi.org/10.1111/j.1365-246X.2004.02405.x.
Hanks, T.C., Kanamori, H., 1979. A moment magnitude scale. J. Geophys. Res. 84, 2348. https://doi.org/10.1029/JB084iB05p02348.
Helmstetter, A., Kagan, Y.Y., Jackson, D.D., 2007. High-resolution time-independent grid based forecast for M $\geq$ 5 earthquakes in California. Seismol. Res. Lett. 78, 78–86.
Hudson, M., Idriss, I., Beikae, 1992. QUAD4M, a Computer Program to Evaluate the Seismic Response of Soil Structures Using Finite Element Procedures and Incorporating a Compliant Base. https://www.researchgate.net/publication/288511774_QUAD4M last seen 28Th September 2022.
Iervolino, I., Galasso, C., Cosenza, E., 2010. REXEL: computer aided record selection for code-based seismic structural analysis. Bull. Earthq. Eng. 8, 339–362.
Iervolino, I., Galasso, C., Paolucci, R., Pacor, F., 2011. Engineering ground motion record selection in the ITalian ACcelerometric Archive. Bull. Earthq. Eng. 9, 1761–1778.
Iervolino, I., Vitale, A., Cito, P., 2021. Empirical assessment of seismic design hazard's exceedance area. Sci. Rep. 11, 18803. https://doi.org/10.1038/s41598-021-98388-9.
Improta, L., Latorre, D., Margheriti, L., Nardi, A., Marchetti, A., Lombardi, A.M., Castello, B., Villani, F., Ciaccio, M.G., Mele, F.M., Moretti, M., the Bollettino Sismico Italiano Working Group, 2019. Multi-segment rupture of the 2016 Amatrice-Visso-Norcia seismic sequence (Central Italy) constrained by the first high-quality catalogue of Early Aftershocks. Sci. Rep. 9, 6921. https://doi.org/10.1038/s41598-019-43393-2.
Itasca Consulting Group, Inc, 2019. FLAC3D — Fast Lagrangian Analysis of Continua in Three-Dimensions, Ver. 7.0. Minneapolis: Itasca.
Kaklamanos, J., Baise, L.G., Boore, D.M., 2011. Estimating unknown input parameters when implementing the NGA ground-motion prediction equations in engineering practice. Earthquake Spectra 27, 1219–1235. https://doi.org/10.1193/1.3650372.
Kawase, H., Aki, K., 1989. A study on the response of a soft basin for incident S, P, and Rayleigh waves with special reference to the long duration observed in Mexico City. Bull. Seismol. Soc. Am. 79, 1361–1382. https://doi.org/10.1785/BSSA0790051361.
Komatitsch, D., Vilotte, J.-P., 1998. The spectral element method: an efficient tool to simulate the seismic response of 2D and 3D geological structures. Bull. Seismol. Soc. Am. 88, 368–392. https://doi.org/10.1785/BSSA0880020368.
Koukouvelas, I.K., 1998. The Egion fault, earthquake-related and long-term deformation, gulf of Corinth, Greece. J. Geodyn. 26 (24), 501–513.
Lanzano, G., Luzi, L., Pacor, F., Felicetta, C., Puglia, R., Sgobba, S., D'Amico, M., 2019. A revised ground-motion prediction model for shallow crustal earthquakes in Italy. Bull. Seismol. Soc. Am. 109 (2), 525–540. https://doi.org/10.1785/0120180210.
Lanzano, G., Luzi, L., D'Amico, V., Pacor, F., Meletti, C., Marzocchi, W., Rotondi, R., Varini, E., 2020. Ground Motion Models for the new seismic hazard model of Italy (MPS19): selection for active shallow crustal regions and subduction zones. Bull. Earthq. Eng. 18, 3487–3516. https://doi.org/10.1007/s10518-020-00850-y.
Lanzo, G., Silvestri, F., Costanzo, A., d'Onofrio, A., Martelli, L., Pagliaroli, A., Sica, S., Simonelli, A., 2011. Site response studies and seismic microzoning in the Middle Aterno valley (L'aquila, Central Italy). Bull. Earthq. Eng. 9, 1417. https://doi.org/10.1007/s10518-011-9278-y.
Lavecchia, G., de Nardis, R., 2010. Seismogenic sources of major earthquakes of the Maiella area (Central Italy): constraints from macroseismic field simulations and regional seismotectonics. UR 4 (01). DPC-INGV project 2007-2009.
Luzi, L., Pacor, F., Puglia, R., Lanzano, G., Felicetta, C., D'Amico, M., Michelini, A., Faenza, L., Lauciani, V., Iervolino, I., Baltzopoulos, G., Chioccarelli, E., 2017. The Central Italy seismic sequence between August and December 2016: analysis of strong-motion observations. Seismol. Res. Lett. 88 (5), 1219–1231. https://doi.org/10.1785/0220170037.
Luzi, L., Lanzano, G., Felicetta, C., D'Amico, M., Russo, E., Sgobba, S., Pacor, F., ORFEUS Working Group 5, 2020. Engineering Strong Motion Database (ESM) (Version 2.0). Istituto Nazionale di Geofisica e Vulcanologia (INGV). https://doi.org/10.13127/ESM.2.
Lysmer, J., Kuhlemeyer, R.L., 1969. Finite Dynamic Model for Infinite Media. J. Eng. Mech. Div. 95, 859–878.
Malagnini, L., Herrman, R.B., 2000. Ground-motion scaling in the region of the 1997 Umbria-Marche earthquake (Italy). Bull. Seismol. Soc. Am. 90, 1041–1051.
Malagnini, L., Akinci, A., Mayeda, K., Munafò, I., Herrmann, R.B., Mercuri, A., 2011. Characterization of earthquake-induced ground motion from the L'Aquila seismic sequence of 2009, Italy. Geophys. J. Int. 184, 325–337.
Manfredi, V., Masi, A., Ozcebe, A., Paolucci, R., Smerzini, C., 2022. Selection and spectral matching of recorded ground motions for seismic fragility analyses. Bull. Earthq. Eng. 20 https://doi.org/10.1007/s10518-022-01393-0.
McGuire, R.K., 1976. FORTRAN computer program for seismic risk analysis. U.S. Geol. Surv. Open-File Rept. 67–76.
Meletti, C., Visini, F., D'Amico, V., Rovida, A., 2016. Seismic hazard in Central Italy and the 2016 Amatrice earthquake. Ann. Geophys. 59, 44. https://doi.org/10.4401/ag-7248.
Meletti, C., Marzocchi, W., D'Amico, V., Lanzano, G., Luzi, L., Martinelli, F., Pace, B., Rovida, A., Taroni, M., Visini, F., Group, M.W, 2021. The new Italian seismic hazard model (MPS19). Ann. Geophys. 64, 112. https://doi.org/10.4401/ag-8579.

Meyer, B., Armijo, R., Massonnet, D., de Chabalier, J.B., Delacourt, C., Ruegg, J.C., Achache, J., Briole, P., Papanastassio, D., 1996. The 1995 Grevena (Northern Greece) earthquake: fault model constrained with tectonic observations and SAR interferometry. Geophys. Res. Lett. 23, 2677–2680.

Miccadei, E., Barberi, R., Cavinato, G.P., 1998. La geologia quaternaria della conca di Sulmona Abruzzo. Geol. Rom. Vol.XXXIV, Italia centrale.

Miccadei, E., Piacentini, T., Barberi, R., 2002. Uplift and local tectonic subsidence in the evolution of intramontane basins: the example of the Sulmona basin (central Apennines, Italy). In: Dramis, F., Farabollini, P., Molin, P. (Eds.), Large-Scale Vertical Movements and Related Gravitational Processes. International Workshop Camerino-Rome, 21–26 June, 1999. Studi Geologici Camerti, pp. 119–134.

Montaldo, V., Faccioli, E., Zonno, G., Akinci, A., Malagnini, L., 2005. Ground-motion predictive relationships for the reference seismic hazard map of Italy. J. Seismol. 9, 295–316.

Montaldo, V., Meletti, C., Martinelli, F., Stucchi, M., Locati, M., 2007. On-Line seismic hazard data for the new Italian building code. J. Earthq. Eng. 11 (119–132), 2007. https://doi.org/10.1080/13632460701280146.

NTC2018, Norme Tecniche per le Costruzioni, 2018. Gazzetta Ufficiale n. 42 S.O. N°8, 20 Febbraio 2018 (in Italian).

Ogata, Y., 1999. Estimating the hazard of rupture using uncertain occurrence times of paleoearthquakes. J. Geophys. Res. 104B (8), 17995–18014.

Olsen, K.B., Schuster, G.T., 1995. Causes of low-frequency ground motion amplification in the Salt Lake Basin: the case of the vertically incident P wave. Geophys. J. Int. 122, 1045–1061. https://doi.org/10.1111/j.1365-246X.1995.tb06854.x.

Pampanin, S., 2012. Reality-check and renewed challenges in Earthquake Engineering: Implementing low-damage structural Systems – from theory to practice. Bull. N. Z. Soc. Earthq. Eng. 45 (4), 137–160. December, ISSN 1174-9875, from Keynote lecture at the WCEE2012.

Panza, G.F., Bela, J., 2020. NDSHA: a new paradigm for reliable seismic hazard assessment. Eng. Geol. 275, 105403 https://doi.org/10.1016/j.enggeo.2019.105403.

Patacca, E., Scandone, P., Di Manna, P., 2021. Geological Map of the Majella Mountain. https://www.isprambiente.gov.it/it/attivita/suolo-e-territorio/cartografia/carta-geologica-della-majella/carta-geologica-della-majella (last check of availability 18 Feb. 2022).

Petersen, M.D., Moschetti, M.P., Powers, P., Mueller, C.S., Haller, K.M., Frankel, A.D., Zeng, Y., Rezaeian, S., Harmsen, S.C., Boyd, O.S., Field, N., Chen, R., Rukstales, K.S., Luco, N., Wheeler, R.L., Olsen, A.H., 2014. Documentation for the 2014 National Seismic Hazard Maps. U.S. Geological Survey, p. 2014.

Petricca, P., Barba, S., Carminati, E., Doglioni, C., Riguzzi, F., 2015. Graviquakes in Italy. Tectonophysics 656, 202–214. https://doi.org/10.1016/j.tecto.2015.07.001.

Petricca, P., Bignami, C., Doglioni, C., 2021. The epicentral fingerprint of earthquakes marks the coseismically activated crustal volume. Earth Sci. Rev. 218, 103667 https://doi.org/10.1016/j.earscirev.2021.103667.

Pizzi, A., Pugliese, G., 2004. InSAR-DEM analyses integrated with geological field methods for the study of long-term seismogenic fault behaviour: applications in the axial zone of the central Apennines (Italy). J. Seismol. 8 (3), 313–329.

Pizzi, A., Falcucci, E., Gori, S., Galadini, F., Messina, P., Di Vincenzo, M., Esestime, P., Giaccio, B., Pomposo, G., Sposato, A., 2010. Active faulting in the Maiella Massif (central Apennines), Italy. GeoActa 9430, 141–158.

Puglia, R., Russo, E., Luzi, L., D'Amico, M., Felicetta, C., Pacor, F., Lanzano, G., 2018. Strong-motion processing service: a tool to access and analyse earthquakes strong-motion waveforms. Bull. Earthq. Eng. https://doi.org/10.1007/s10518-017-0299-z.

Puliti, I., Pizzi, A., Gori, S., Falcucci, E., Galadini, F., Maceroni, D., Moro, M., Saroli, M., 2021. New Paleoseismological Constraints of Late Holocene Earthquakes along the Mt. Morrone Fault (Sulmona Basin, Abruzzi Apennines, Italy). 90° Congresso Della Società Geologica Italiana, Trieste, 14–16 Settembre 2021. Riassunti delle Comunicazioni, p. 217. https://doi.org/10.3301/ABSGI.2021.03.

Rinaldini, A., Grillo, A., Marino, A., 2007. Local seismic amplification analysis in the industrial area of Sulmona, Central Italy. In: Earthquake Resistant Engineering Structures VI. Presented at the ERES 2007. WIT Press, Bologna, Italy, pp. 215–224. https://doi.org/10.2495/ERES070211.

Romano, M.A., de Nardis, R., Lavecchia, G., Garbin, M., Peruzza, L., Priolo, E., Romanelli, M., Ferrarini, F., 2013. Preliminary analysis of the microearthquakes-faults association in the Sulmona basin central Apennines, Italy. Rend. Online Soc. Geol. It. 29, 150–153.

Rovida, A., Locati, M., Camassi, R., Lolli, B., Gasperini, P., 2021. CPTI15, the 2015 version of the Parametric Catalogue of Italian Earthquakes. Istituto Nazionale di Geofisica e Vulcanologia (INGV), Rome. https://doi.org/10.6092/INGV.IT-CPTI15.

Sgobba, S., Puglia, R., Pacor, F., Luzi, L., Russo, E., Felicetta, C., Lanzano, G., D'Amico, M., Baraschino, R., Baltzopoulos, G., Iervolino, I., 2019. REXELweb: A tool for selection of ground-motion records from the Engineering strong Motion database (ESM). In: 7th International Conference on Earthquake Geotechnical Engineering (ICEGE) 17–20 June 2019, Roma, Italy. 8(i), pp. 4947–4953.

Sgobba, S., Felicetta, C., Russo, E., D'Amico, M., Lanzano, G., Pacor, F., Luzi, L., Baraschino, R., Baltzopoulos, G., Iervolino, I., 2021a. The online graphical user interface of REXELweb for the selection of accelerograms from the engineering strong motion database (ESM). In: 39° Convegno nazionale Gruppo Nazionale di Geofisica della Terra Solida 22–24 giugno 2021 online.

Sgobba, S., Felicetta, C., Lanzano, G., Ramadan, F., D'Amico, M., Pacor, F., 2021b. NESS2.0: an Updated Version of the Worldwide Dataset for Calibrating and Adjusting Ground-Motion Models in near Source. Bull. Seismol. Soc. Am. https://doi.org/10.1785/0120210080.

Sgobba, S., Lanzano, G., Pacor, F., Felicetta, C., 2021c. An Empirical Model to Account for Spectral Amplification of Pulse-like Ground Motion Records. Geosciences 11, 15. https://doi.org/10.3390/geosciences11010015.

STACEC, srl, 2017. LSR 2d (Local Seismic Response 2d). Bovalino, RC (Italy).

Stucchi, M., Meletti, C., Montaldo, V., Crowley, H., Calvi, G.M., Boschi, E., 2011. Seismic Hazard Assessment (2003-2009) for the Italian Building Code. Bull. Seismol. Soc. Am. 101, 1885–1911. https://doi.org/10.1785/0120100130.

Valentini, A., Visini, F., Pace, B., 2017. Integrating faults and past earthquakes into a probabilistic seismic hazard model for peninsular Italy. Nat. Hazards Earth Syst. Sci. 17 (11), 2017–2039. https://doi.org/10.5194/nhess-17-2017-2017.

Valoroso, L., Chiaraluce, L., Piccinini, D., Di Stefano, R., Schaff, D., Waldhauser, F., 2013. Radiography of a normal fault system by 64,000 high-precision earthquake locations: the 2009 L'Aquila (Central Italy) case study. J. Geophys. Res. Solid Earth 118, 1156–1176.

Villani, M., Faccioli, E., Ordaz, M., Stupazzini, M., 2014. High-Resolution Seismic Hazard Analysis in a complex Geological Configuration: the Case of the Sulmona Basin in Central Italy. Earthquake Spectra 30, 1801–1824. https://doi.org/10.1193/1112911EQS288M.

Vittori, E., Cavinato, G.P., Miccadei, E., 1995. Active faulting along the northeastern edge of the Sulmona basin, central Apennines, Italy. In: "Perspective in paleoseismology" a cura di Serva L. E Burton Slemmons D. Ass. of Engin. Geol. Special Publication, 6, pp. 115–126 sudbury.

Vucetic, M., 1994. Cyclic threshold shear strains in soils. ASCE, J. Geotechn. Eng. 120 (12), 2208–2228.

Wells, D.L., Coppersmith, K.J., 1994. New empirical relationships among magnitude, rupture length, rupture width, rupture area, and surface displacement. Bull. Seismol. Soc. Am. 84, 974–1002 (Appendix. Supplementary materials).

Yelikaya, T., Mercanlig, O., 2020. Three Dimensional Physics Based Earthquake Simulation Scenarios for the Sulmona Basin (Abruzzo, Italy), in: Phd Dissertation. Politecnico Milano, p. 196.